

## A Local Energetics Analysis of the Life Cycle Differences between Consecutive, Explosively Deepening, Continental Cyclones

STEVEN G. DECKER AND JONATHAN E. MARTIN

*Department of Atmospheric and Oceanic Sciences, University of Wisconsin—Madison, Madison, Wisconsin*

(Manuscript received 22 March 2004, in final form 22 July 2004)

### Abstract

Local energetics diagnostics of the life cycles of consecutive, explosively deepening, extratropical cyclones that migrated across central North America in April 2001 are presented. Both storms developed rapidly and followed nearly identical tracks through the region. Despite similar mature-stage intensities, the two storms underwent vastly different evolutions during cyclolysis; the first decayed as rapidly as it had developed, and the second decayed very slowly. Examination of the volume-integrated eddy kinetic energy (EKE) budget for each storm reveals that the sea level pressure minimum associated with the first cyclone developed well after its associated EKE center had reached its maximum intensity. In contrast, the second cyclone's sea level pressure minimum developed much more in concert with the development of its associated EKE center. As a consequence, the first cyclone began losing EKE through downstream energy fluxes even as it was developing at the surface, whereas the second cyclone did not disperse EKE downstream until later in its life cycle. Consideration of the EKE budget results in terms of baroclinic wave packets demonstrates that the first cyclone developed and decayed on the upstream edge of a wave packet, whereas the second cyclone developed in the midst of a wave packet, only decaying once it had reached the upstream edge. Thus, it is suggested that postmature phase decay is dynamically linked to a cyclone's position in a given wave packet.

### 1. Introduction

The growth and decay of midlatitude cyclones have been central questions in synoptic–dynamic meteorology for nearly two centuries (Kutzbach 1979). A major synthesis of much of the prior thinking was manifest in the Norwegian Cyclone Model (NCM) of the “Bergen School,” the history of which is described by Volkert (1999). The genius of this model was that it depicted several discrete stages of the midlatitude cyclone (and the significant weather associated with each) in the context of an identifiable cyclone life cycle. Though the model was primarily descriptive, it did suggest that a conversion of the potential energy present in the characteristic horizontal temperature contrasts served as the cyclone's primary mechanism for kinetic energy growth. The theoretical work of Charney (1947) and Eady (1949), focusing on the instability of simple baroclinic flows, led to a greater understanding of the growth of the midlatitude cyclone.

An intriguing component of the NCM, not considered in these baroclinic instability theories, was the no-

tion of “cyclone families” in which one storm, in a sequence, was thought to be physically related to another. This suggestion has subsequently been considered from the perspective of cyclone energetics. Sixty years ago, Namias and Clapp (1944), hinted at the importance of energy transfer between discrete systems. A substantive analysis of the sources and sinks of energy that result in the growth and decay of individual baroclinic systems, a method later referred to as “local energetics diagnostics,” was originally employed to understand the manner by which such systems interacted with the general circulation (e.g., Petterssen and Smebye 1971). Later studies examined the kinetic energy budget of various flow regimes. In one such study over North America, Kung (1977) found evidence that the quantity now called ageostrophic geopotential flux (AGF) might play an important role in cyclone life cycles, but, in general, studies such as that one were limited by their reliance on purely observational data, which could not resolve the ageostrophic wind. With the arrival of high-resolution gridded datasets provided by model initializations and reanalysis projects, the local energetics method matured in the early 1990s through the work of Orlanski and collaborators (Orlanski and Katzfey 1991; Orlanski and Chang 1993; Chang and Orlanski 1993; Orlanski and Sheldon 1993). These studies confirmed what had been alluded to pre-

---

*Corresponding author address:* Jonathan E. Martin, Dept. of Atmospheric and Oceanic Sciences, University of Wisconsin—Madison, 1225 W. Dayton St., Madison, WI 53705.  
E-mail: jon@aos.wisc.edu

viously: energy transfers between distinct midlatitude synoptic-scale disturbances control a large part of the local energetics, at least in specific cases. Orlanski and Sheldon (1995) codified this view by defining a new paradigm whereby baroclinic life cycles could be understood in large part simply by considering energy transfers between discrete systems. Chang (2000) found that these transfers of energy often dominated other processes whenever the disturbances were organized into coherent wave packets.

In this study, we apply local energetics diagnostics to the life cycles of two consecutive midlatitude cyclones that ravaged portions of central North America during April 2001. The approach taken is a novel one regarding midlatitude-cyclone life cycles. Although local energetics diagnostics have been employed to explain energy sources for a variety of *individual* storms, to our knowledge they have not been used in an attempt to diagnose the observed differences in evolution between consecutive cyclones. The two cyclones investigated here were notable in that, despite similarities in their surface cyclogenesis characteristics, their decay stages were remarkably different. The paper is organized as follows. Section 2 provides some theoretical background on local energetics, downstream development, and wave packets. Section 3 recaps the synoptic evolution of the two cyclones, showing that the first storm experienced rapid decay, whereas the second storm did not. Then, section 4 describes the method employed in

the local energetics analysis of the two cyclones, and section 5 presents the results of that analysis. Section 6 discusses the results and offers concluding remarks.

## 2. Theoretical background

### a. Equations and definitions

The physical quantity of interest in local energetics is eddy kinetic energy per unit mass (EKE). Defining EKE requires that the flow field be partitioned into mean and eddy components. Several choices exist for defining a mean state. For instance, Orlanski and Sheldon (1993) use a zonal mean. In the present study, we adopt a time mean and use the following notation to denote the partitioning:

$$A = A_m + a, \quad (1)$$

where  $A$  represents any scalar or vector field, subscript  $m$  refers to the time-mean part, and lowercase indicates the eddy part. EKE is calculated as  $(u^2 + v^2)/2$  (where  $u$  and  $v$  are the zonal and meridional velocity components, respectively) and has units of joules per kilogram.

The EKE tendency equation is the fundamental tool used in this study. Lackmann et al. (1999) and McLay and Martin (2002) provide a derivation of this equation (not replicated here) wherein the EKE tendency in isobaric coordinates is given by

$$\begin{aligned} \frac{\partial(\text{EKE})}{\partial t} = & - \nabla \cdot (\mathbf{v}\phi)_a - \omega\alpha - \mathbf{V}_3 \cdot \nabla_3(\text{EKE}) - \mathbf{v} \cdot (\mathbf{v}_3 \cdot \nabla_3)\mathbf{V}_m + \mathbf{v} \cdot \frac{\mathbf{E}}{(\mathbf{v}_3 \cdot \nabla_3)\mathbf{v}} \\ & + \mathbf{v} \cdot \mathbf{f} + \frac{\tan\Theta}{R_e} (u^2 V_m - uvU_m - u\bar{u}\bar{v} + \overline{vu^2}) + \text{Residual}. \end{aligned} \quad (2)$$

In this equation,  $\alpha$  is the specific volume,  $\mathbf{f}$  refers to the eddy frictional force (per unit mass),  $\Theta$  is the latitude,  $R_e$  is the earth's radius,  $\mathbf{V}_3$  is the 3D total wind,  $\mathbf{v}_3$  is the 3D eddy wind, and  $\mathbf{v}$  is the 2D eddy wind. Overbars represent time means of combined eddy quantities. The significance of the subscript  $a$  is shown below. Other notation is standard. Table 1 provides the correspon-

dence between the various terms and the names and abbreviations used in this paper. Each term has a distinct physical meaning.

### b. Physical interpretations

Terms A and B each can be shown to represent parts of the same physical process, the conversion of potential energy to kinetic energy through work done by the pressure gradient force (PGF). We call  $(\mathbf{v}\phi)_a$  the ageostrophic geopotential flux vector, and, as in Orlanski and Sheldon (1993), it is defined as

$$(\mathbf{v}\phi)_a = \mathbf{v}\phi - \mathbf{k} \times \nabla \frac{\phi^2}{2f(\Theta)}, \quad (3)$$

where  $f$  is the Coriolis parameter and  $\mathbf{k}$  is the unit vector in the vertical direction. As shown by Orlanski and Katzfey (1991), this vector represents that portion of

TABLE 1. The correspondence between terms in the EKE tendency equation and their common names. Abbreviated names used in the text are given in parentheses.

Term	Name
A	Ageostrophic geopotential flux convergence (AGFC)
B	Baroclinic generation/conversion (Barc)
C	Advection (Adv)
D	Barotropic generation/conversion (Bart)
E	Time-mean stress (TMS)
F	Friction (Fric)
G	Curvature (Curv)
H	Residual (Res)

the instantaneous transport of EKE that is not due to advection, but instead to a radiation or dispersion of energy to another location. Term B is the classic baroclinic generation term, by which rising warm air or sinking cold air produces EKE at the expense of eddy available potential energy. Orlanski and Katzfey (1991) argue that terms A and B should be roughly equal and opposite in equivalent barotropic (i.e., occluded) structures. Evidence for this correspondence between A and B will be apparent during the analysis.

The other terms are commonly less important mechanisms for cyclone growth and decay. Term C, the advection, may be large locally but is small when regionally integrated. The barotropic generation term (D) and its close cousin the time-mean stress term (E) represent energy exchanges involving the eddy flow. Also known as the Reynolds stress term, the barotropic generation term represents the EKE tendency due to the conversion of kinetic energy between the eddy and mean flow. The time-mean stress term is a conversion between EKE and  $U_m u + V_m v$ , the eddy-mean correlation, but in this case the time average of the term is zero, as is the time average of the eddy-mean correlation. The curvature term (G) describes the same conversion but arises as a correction term that accounts for the fact that the analysis uses Cartesian coordinates instead of spherical coordinates.

Given the dataset (more thoroughly described in the next section), the true value of the friction term (F) is unknown. However, a model-derived planetary boundary layer height is included in the dataset. Thus, the frictional force was approximated by setting it to zero outside the boundary layer while assuming a three-way force balance among the pressure gradient force, Coriolis force, and friction inside the layer.<sup>1</sup>

The final term (H), the residual, is defined as the difference between the observed and calculated EKE tendencies and is computed following the method of McLay and Martin (2002). In addition to including the effects of any processes ignored in deriving the EKE tendency equation (e.g., molecular dissipation), this term also contains contributions from numerical errors in the calculation of all of the other terms in the equation, discretization errors, and errors in the dataset.<sup>2</sup>

### c. Downstream development

The idea of downstream development has been discussed at least as early as Namias and Clapp (1944). Chang and Orlanski (1993) showed that downstream development occurred in idealized simulations of baro-

clinic waves. Orlanski and Sheldon (1993) called this “downstream baroclinic development” to emphasize that baroclinic processes were involved in the case they studied. Though that is true for the current work as well, the term “downstream development” is used here.

Orlanski and Sheldon (1995) established the downstream development paradigm in terms of local energetics. Their conceptual model contained three stages of downstream development. In the first stage, a pre-existing EKE center downstream of a trough weakens through the dispersal of AGF through the downstream ridge. The convergence of that AGF produces a new EKE center downstream. In the second stage, this new center grows through baroclinic conversion while sending AGF through the trough to yet another developing EKE center. Last, in the third stage, the EKE center west of the trough decays. The EKE center east of the trough subsequently reaches maximum intensity, with the aid of baroclinic conversion, and begins to send energy downstream itself. The first stage can then occur again; the cycle potentially repeats.

In fact, the cycle often does repeat numerous times, and the result can be a coherent train of ridges and troughs limited in zonal extent. The name “wave packet” is given to these localized, coherent wave trains. Lee and Held (1993) provided observational and idealized modeling evidence of the existence of such wave packets, and Chang and Yu (1999) and Chang (1999) provided some basic characteristics of observed wave packets. One important characteristic of wave packets is that their group velocity is greater than the phase speed of the individual ridges and troughs contained within the packet. Consistent with this characteristic, ridges and troughs develop on the leading (downstream) side of the wave packet, move upstream relative to the wave packet, and decay on the trailing (upstream) side of the wave packet. Chang and Orlanski (1994) demonstrated that an energy flux vector similar to the AGF vector accurately captures the group velocity of both idealized and observed wave packets. Chang (2000) showed that downstream development occurred within his observed wave packets much of the time and that almost all trough developments due to downstream development led to surface cyclogenesis. The ideas and related diagnostics described in this section are now applied to an examination of two consecutive explosive cyclones that developed in central North America in April 2001.

## 3. Synoptic overview

During the second week of April 2001, two powerful cyclones developed over and traveled across central North America, one immediately following the other. In this study, these storms will be referred to as storm 1 (6–9 April 2001) and storm 2 (10–14 April 2001). The two storms evolved out of broadly similar

<sup>1</sup> In the strong cyclonic systems we consider here, the centrifugal force can be considerable and may lead to an incorrect estimate of the eddy frictional force.

<sup>2</sup> Because the dataset employed is an analysis, it is not necessarily energetically consistent, as a consequence of observational increments.

large-scale environments, as shown in Fig. 1. In each case, the incipient storm was associated with a slightly positively tilted upper-tropospheric trough over the southwestern United States and a broad anticyclonically curved jet arcing northeastward toward New England. In addition, large ridges existed over the eastern North Pacific Ocean, while the northern stream possessed troughs over southwestern and southeastern Canada, with ridges near Hudson Bay. Though broadly similar, the two environments possessed some differences. The most obvious difference between the two flow patterns was the vastly dissimilar jet strength off the coast of British Columbia. In the precursor envi-

ronment to storm 1, the jet maximum approached  $83 \text{ m s}^{-1}$ . The corresponding jet maximum in storm 2's case was a weaker  $52 \text{ m s}^{-1}$ . Another difference between the two environments was the sharper curvature at the base of the upper-level trough associated with storm 1.

Both storms reached minimum sea level pressures (SLPs) near or below 980 hPa, and their maximum deepening rates were impressive. Figure 2 displays the tracks and SLP minima of the two cyclones. Storm 1 (2) deepened at a maximum rate of 1.24 (1.30) bergerons [as defined by Sanders and Gyakum (1980)]. Thus, both qualified as explosively deepening cyclones—relatively rare events over the continent. The two storms were

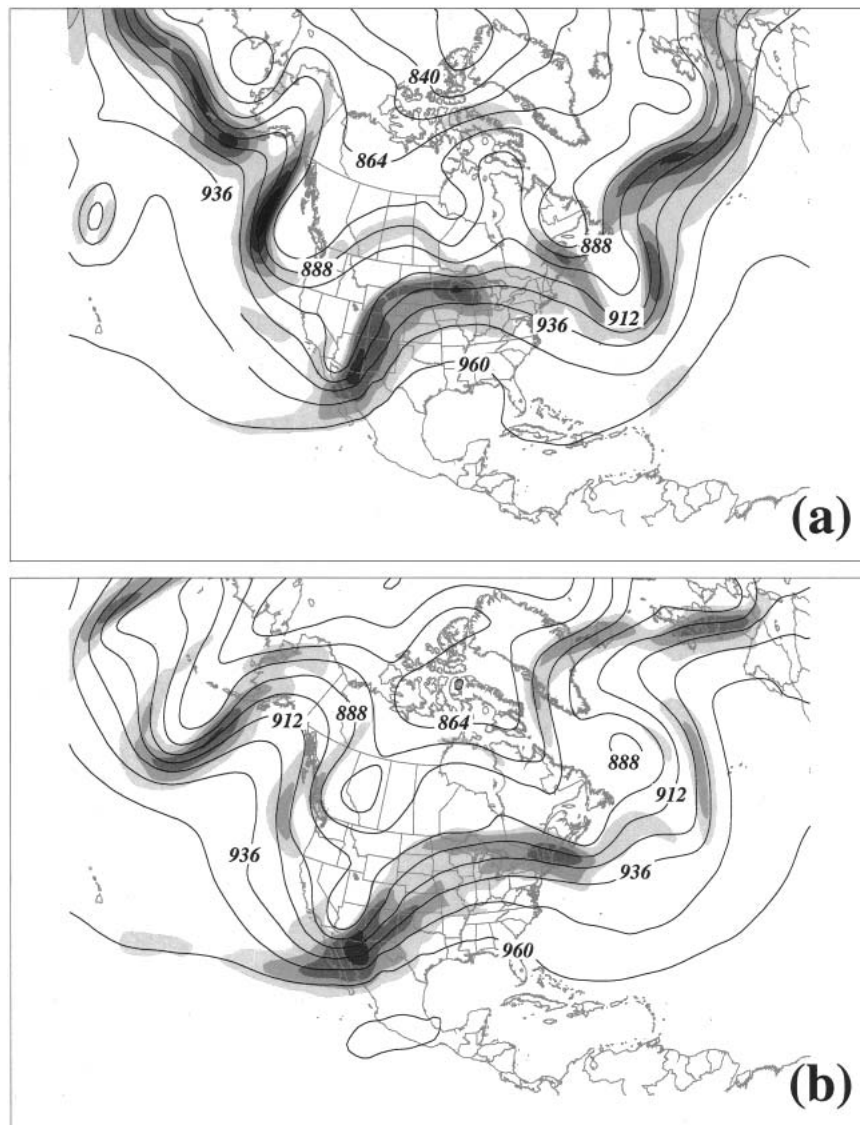


FIG. 1. The 300-hPa geopotential heights and isotachs from the NCEP FNL analysis valid at (a) 1200 UTC 6 Apr 2001 and (b) 1800 UTC 10 Apr 2001. Geopotential heights (solid lines) are contoured every 12 dam. Isotachs are shaded in increments of  $10 \text{ m s}^{-1}$ , beginning with  $35 \text{ m s}^{-1}$ . The two times correspond to 24 h prior to each storm reaching its respective sea level pressure minimum.



FIG. 2. Position of sea level pressure minima at 12-h intervals for storm 1 (dark dots and path; from 1200 UTC 6 Apr to 1200 UTC 9 Apr 2001) and storm 2 (light dots and path; from 1200 UTC 10 Apr to 1200 UTC 13 Apr 2001). Values of SLP at each time for each storm are taken from the NCEP FNL analysis at the respective time.

also similar with respect to the Konrad and Colucci (1988) bomb classifications. Each storm can be classified as a ridge-building closed low, a distinction enjoyed by only 11% of bombs. It is clear that these two bombs were similarly exceptional.

Despite these similarities, differences emerged between the two storms during their decay stages. Storm 1 filled by 28.3 hPa over the 48 h subsequent to its most rapid deepening, whereas storm 2 filled by only 6.4 hPa over the 48 h subsequent to its most rapid deepening. As a result, storm 1 had an SLP of less than 1000 hPa for about 58 h, whereas storm 2 maintained an SLP of less than 1000 hPa for 98 h. A brief overview of each storm's evolution is presented next.

#### a. Storm 1

Storm 1 deepened explosively in the lee of the Rocky Mountains on 6 April, accompanied by a mainly non-tornadic severe-weather outbreak over the Great Plains. While moving northeastward into Canada, the cyclone continued to produce damage, not through thunderstorms, but rather through wind gusts exceeding hurricane force that were related to the tight pressure gradient. The surface map valid at the time of storm 1's maximum intensity illustrates the extreme nature of the storm (Fig. 3). Note the sustained wind of 40 kt ( $21 \text{ m s}^{-1}$ ) reported at Algona, Iowa (AXA), for instance. The thermal contrasts associated with both the cold and warm fronts were well defined. Temperatures dropped nearly  $16^\circ\text{C}$  across the cold front from Springfield, Missouri (SGF), to Garden City, Kansas (GCK), but there was little cloudiness and no precipitation accompanying the front. Along the warm front, temperatures plunged  $12^\circ\text{C}$  between Moline, Illinois (MLI), and Lone Rock,

Wisconsin (LNR). Unlike the cold front, the warm front was associated with a substantial cloud and precipitation shield.

Examination of the middle and upper troposphere indicates that, at this point in its evolution, storm 1 was vertically stacked from the surface to at least 500 hPa (Fig. 4), was removed from the peak of the warm sector (Fig. 4b), and was located in the left exit region of a compact jet streak (Fig. 4a). At 500 hPa, an intense elliptical absolute vorticity maximum was located just southeast of the cyclone center (Fig. 4b). Intense cyclonic vorticity advection downstream of that feature, combined with localized warm advection in the lower troposphere, provided forcing for vigorous vertical motions that produced the clouds and precipitation across the Upper Midwest (Fig. 3). In contrast, the region along the cold front experienced little temperature or vorticity advection, consistent with the scarcity of clouds and absence of precipitation across that area.

#### b. Storm 2

Storm 2 also deepened explosively in the lee of the Rockies, and again a severe-weather outbreak simultaneously occurred across the Great Plains. During the early morning hours of 11 April, numerous tornadoes touched down across eastern Oklahoma and Kansas, resulting in six injuries and one fatality. By noontime, the severe weather reached Iowa, with 32 tornadoes reported across that state. In addition to the severe storms, blizzard conditions on the west side of the cyclone closed Denver International Airport in Colorado for the first time in its history and knocked out power to 220 000 customers in Denver (NCDC 2001). Meanwhile, strong winds again blew across a large portion of the country. The surface map valid at the time of the Iowa tornado outbreak (and at the time of storm 2's maximum intensity) shows these strong surface winds (Fig. 5). Although the blizzard had subsided near Denver by this time, the town of Sidney, Nebraska (SNY), reported heavy snow with 40-kt ( $21 \text{ m s}^{-1}$ ) winds, while Springfield, Colorado (SPD), reported sustained winds of 50 kt ( $26 \text{ m s}^{-1}$ ). Both the cold and warm fronts were robust as temperatures decreased by  $17^\circ\text{C}$  across the cold front between Childress, Texas (CDS), and Springfield, Colorado, and decreased by  $9^\circ\text{C}$  across the warm front between Aurora, Illinois (ARR), and Watertown, Wisconsin (RYV). Unlike storm 1, storm 2 was characterized by precipitation along both the cold front (aloft) (not shown) and warm front.

Storm 2 was also vertically stacked, to at least 300 hPa, at its time of maximum intensity (Fig. 6). As in storm 1, the warm front, stretching from the Great Lakes southwestward to the cyclone center (Fig. 6b), was the dominant thermal structure in the lower troposphere. The 500-hPa vorticity maximum was comma shaped (Fig. 6b), with the maximum vorticity nearly

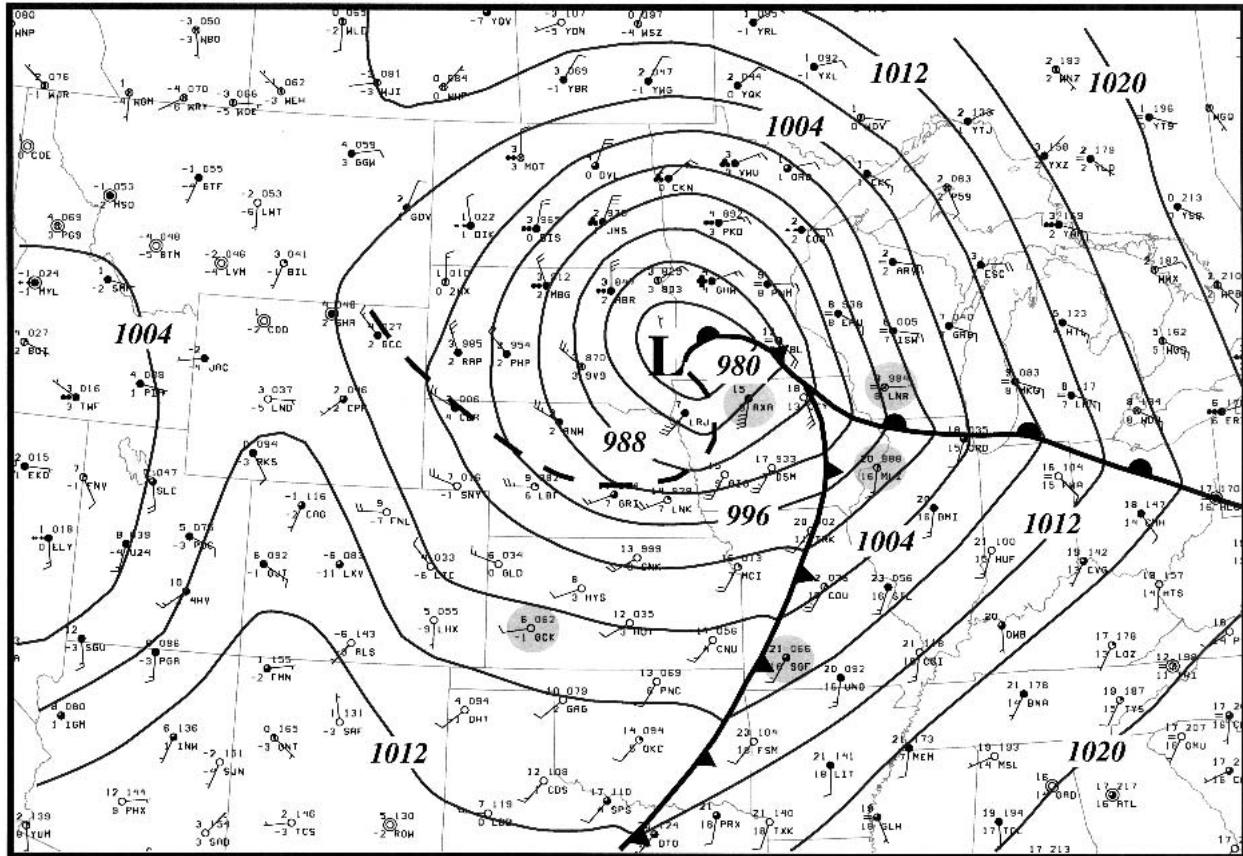


FIG. 3. Sea level pressure analysis at 1200 UTC 7 Apr 2001. Solid lines are sea level isobars, contoured every 4 hPa. For each station, the following data are shown: temperature ( $^{\circ}\text{C}$ ; to the upper left of the station symbol), dewpoint ( $^{\circ}\text{C}$ ; to the lower left of the station symbol), sea level pressure ( $10 \times \text{hPa}$ , dropping the leading 9 or 10; to the upper right of the station symbol), station identifier, wind speed and direction, sky cover, and present weather. Wind speeds are indicated: a circle around station circle = calm, shaft and no barb  $< 2.5 \text{ m s}^{-1}$ , short barb =  $2.5 \text{ m s}^{-1}$ , long barb =  $5 \text{ m s}^{-1}$ , flag =  $25 \text{ m s}^{-1}$ .

collocated with the geopotential minimum. In contrast to storm 1, there was an extensive jet located south of the cyclone (Fig. 6a), although its maximum speed was less than in the case of storm 1.

#### 4. Analysis methods

The mean state in this study was calculated using a 28-day average centered on the given analysis time (0000, 0600, 1200, or 1800 UTC). Each analysis time thus has a different mean associated with it, but the mean window is long enough that differences from one analysis time to the next, or between storms, are negligible. Means are computed for a given hour using data valid only at that hour over the 28-day period. This removes any diurnal cycle from the eddy components. Errors due to the slowly varying mean become part of the residual term.

Terms such as ageostrophic geopotential flux convergence (AGFC) cannot be computed accurately from standard observations alone. Thus, the National Cen-

ters for Environmental Prediction (NCEP) “FNL” analyses available from the National Center for Atmospheric Research (NCAR) were used to construct the local energetics diagnostics. NCAR provides the FNL dataset on a  $1^{\circ} \times 1^{\circ}$  cylindrical equidistant grid, with 50-hPa grid spacing in the vertical direction between 100 and 900 hPa and 25-hPa grid spacing between 900 and 1000 hPa. The dataset also supplies values of necessary variables at the surface, along with boundary layer heights.

An advantage of the local energetics approach is that one can calculate the various terms in the EKE tendency equation at each vertical level and then can perform a vertical average for each quantity without losing much information about the energetics. This obviates the need to examine cross sections or multiple levels in many instances. The vertical average is defined as

$$\bar{A} = \frac{1}{z_{\text{top}} - z_{\text{sfc}}} \int_{z_{\text{sfc}}}^{z_{\text{top}}} \rho A \, dz, \quad (4)$$

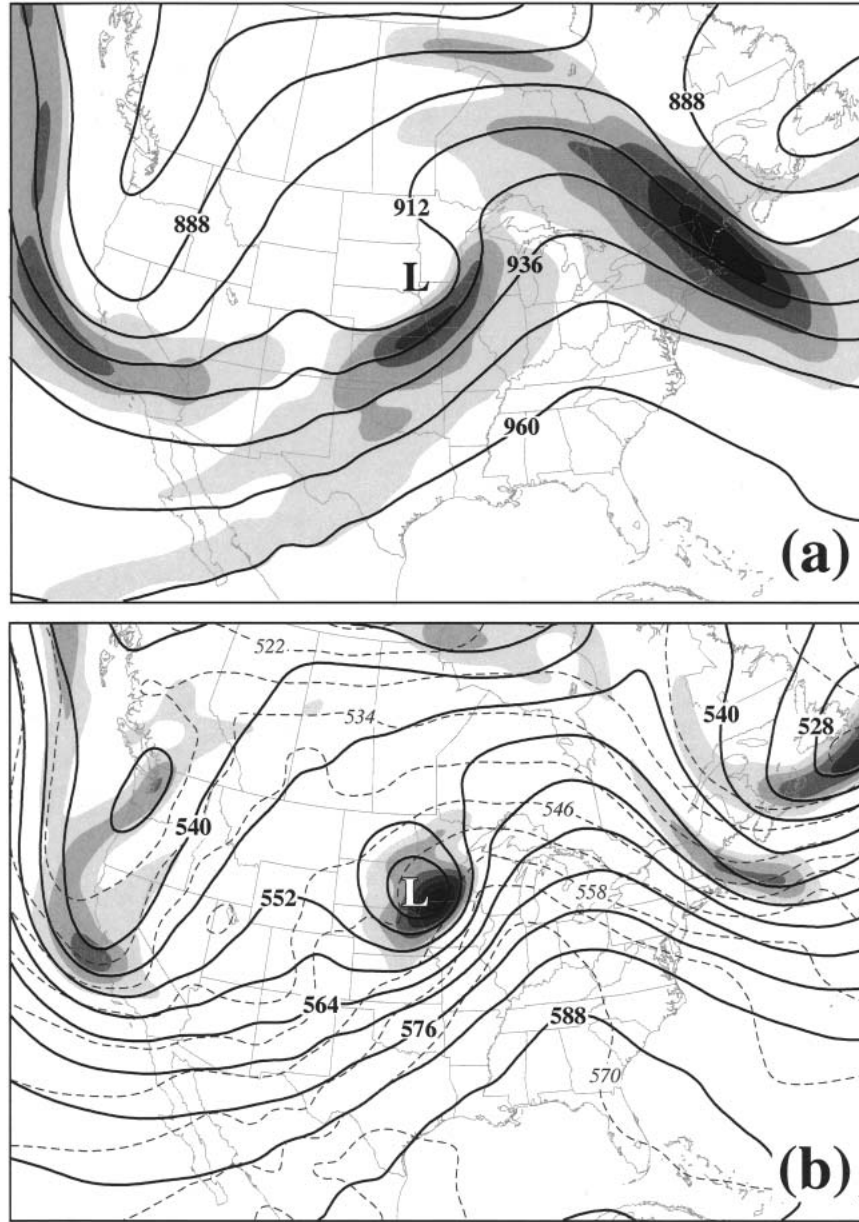


FIG. 4. (a) The 300-hPa geopotential height and isotachs from the NCEP FNL analysis valid at 1200 UTC 7 Apr 2001. Geopotential heights (solid lines) are contoured every 12 dam. Isotachs are shaded in increments of  $10 \text{ m s}^{-1}$ , beginning at  $35 \text{ m s}^{-1}$ . The boldface “L” indicates the position of the sea level pressure minimum at this time. (b) The 500-hPa geopotential height, absolute vorticity, and 1000–500-hPa thickness from the NCEP FNL analysis valid at 1200 UTC 7 Apr 2001. Geopotential height (solid lines) is contoured every 6 dam. Absolute vorticity is shaded in increments of  $5 \times 10^{-5} \text{ s}^{-1}$ , beginning at  $15 \times 10^{-5} \text{ s}^{-1}$ . The 1000–500-hPa thickness (dashed lines) is contoured every 6 dam. The white “L” indicates the position of the sea level pressure minimum at this time.

where  $A$  refers to any variable and  $\rho$  is density. For EKE,  $\bar{A}$  has units of joules per meter cubed. Here,  $z_{\text{sfc}}$  is the surface elevation, and  $z_{\text{top}}$  was chosen to be the geopotential height of the 100-hPa surface.

Volume integrals were computed using the  $135 \text{ J m}^{-3}$  contour of the vertically averaged EKE surrounding

the EKE center of interest as the horizontal boundary. In mathematical terms, then, the volume integral for variable  $A$  is

$$\iiint A dV = \iint_Q (z_{\text{top}} - z_{\text{sfc}}) \bar{A} d\sigma, \quad (5)$$

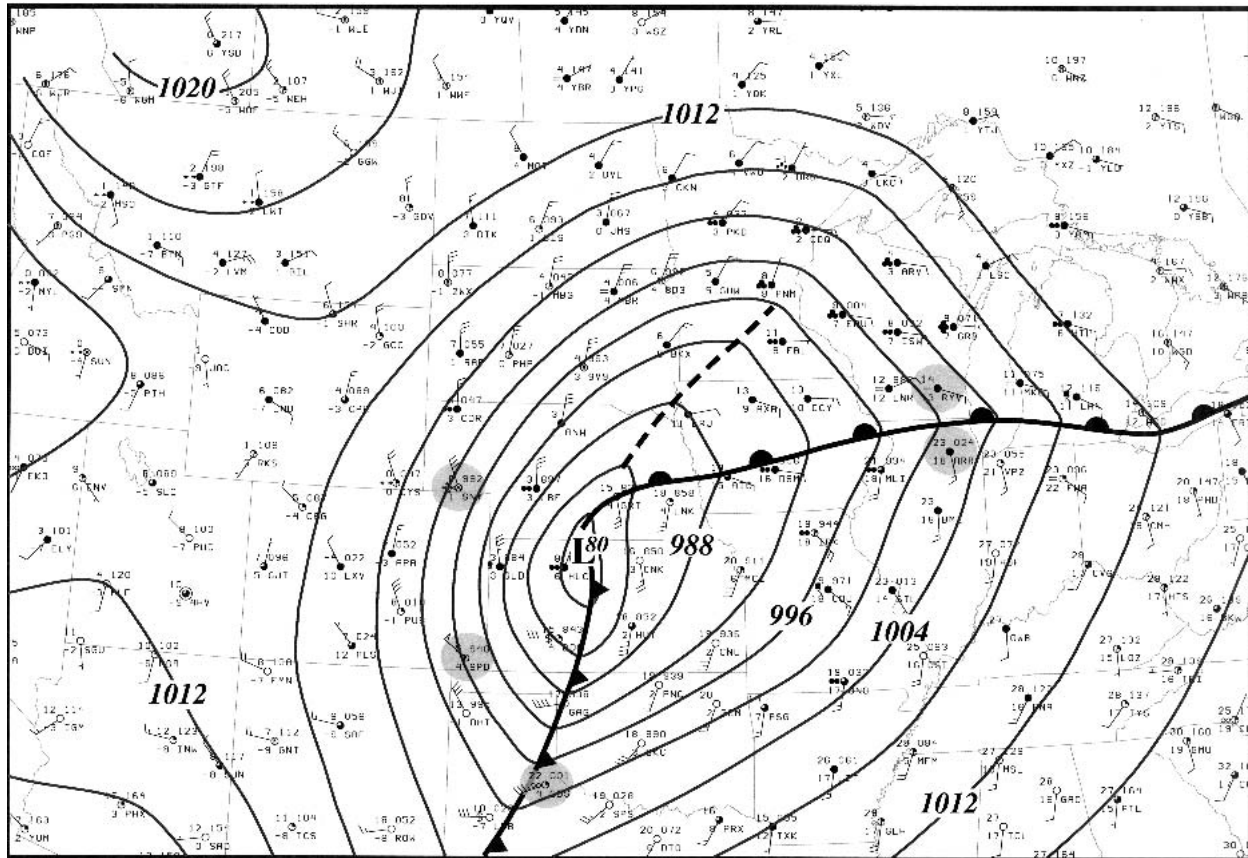


FIG. 5. As for Fig. 3 but at 1800 UTC 11 Apr 2001. The thick dashed line indicates the position of a sea level pressure trough.

where  $d\sigma$  is an area element and the region  $Q$  is enclosed by the  $135 \text{ J m}^{-3}$  contour. The purpose of the volume integrals is to compactly quantify the evolution of the EKE budget terms over the life cycles of the two cyclones of interest. Although the choice of bounding contour seems arbitrary, in fact there is little leeway involved. The contour must have a value large enough to keep the EKE center of interest distinct from surrounding centers yet small enough to exist during the early growth and late decay stages of the center. In order to treat each cyclone similarly, these conditions must hold for both cyclones. The  $135 \text{ J m}^{-3}$  contour clearly stands out in the face of these considerations. Other choices for the bounding contour were tried, but there were no qualitative differences observed in the results.

Because a bounding contour is not a material surface, volume integrals do not provide a complete explanation for the growth and decay of any energy center. No attempt is made to calculate the volume-integrated EKE tendency due to flow across the bounding contour or the 100-hPa surface. In addition, the very early (late) stages of growth (decay) are not considered, because the energy centers' maxima do not exceed  $135 \text{ J m}^{-3}$  during those stages. Despite these limitations, we as-

sume that the implications gleaned from the volume integrals are valid as long as the residual remains small. Last, it is not clear that import of energy from upstream disturbances can necessarily influence a depression in the sea level isobars, and the subsequent analyses are not meant to imply such.

## 5. Results

### a. Storm-1 EKE evolution

Let us now examine the evolution of the eddy kinetic energy and ageostrophic geopotential fluxes over the lifetimes of the two cyclones, beginning with storm 1 (Fig. 7). The EKE center associated with storm 1 (center C) first develops at  $D - 4$ ,<sup>3</sup> which corresponds to 1200 UTC 3 April (Fig. 7a). Note how an EKE center near the Aleutian Islands (center A) disperses its energy downstream to a center off the coast of Washington (center B). Dispersion from this center in turn feeds the growing storm-1 center. This train of EKE centers

<sup>3</sup> In general, the following notation is used:  $D - x$  refers to times  $x$  days before a storm's minimum SLP,  $D_0$  refers to the time of a storm's minimum SLP, and  $D + y$  refers to times  $y$  days after a storm's minimum SLP.

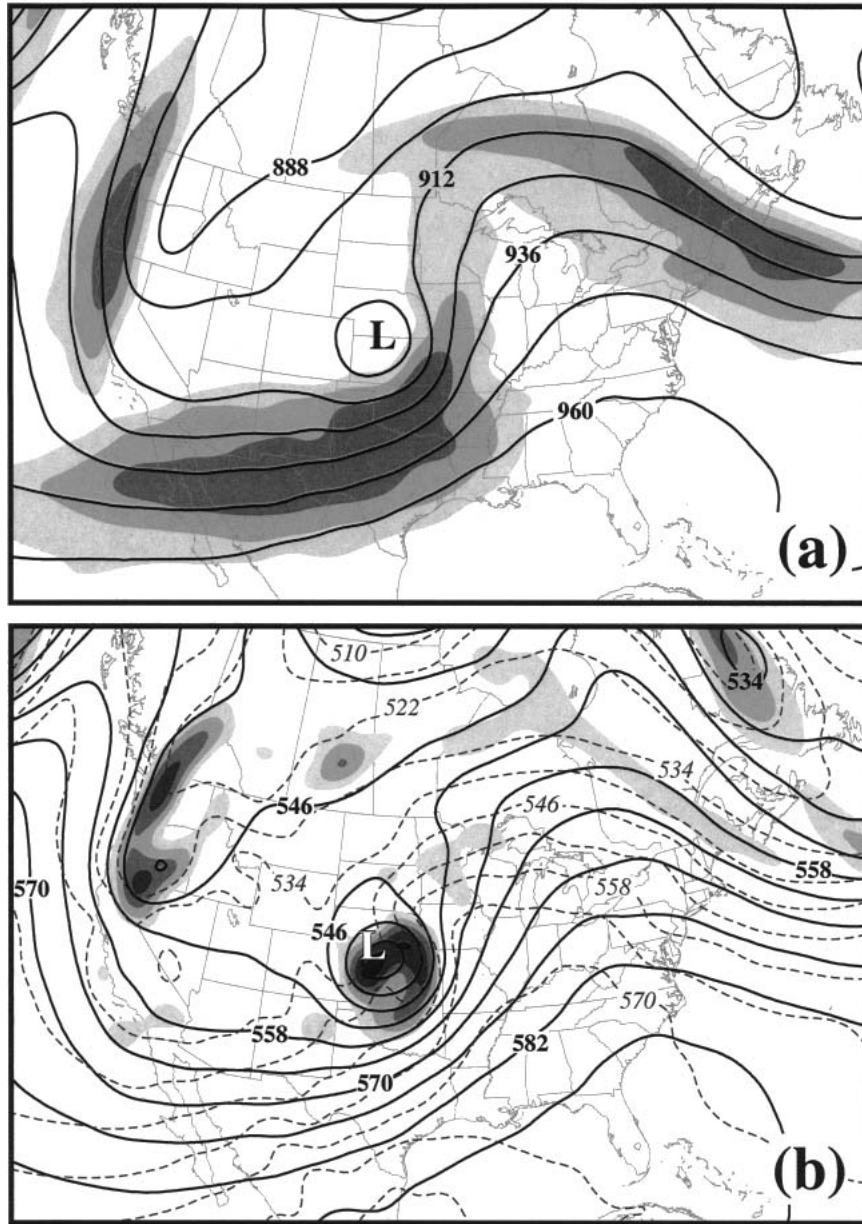


FIG. 6. (a) As in Fig. 4a but from the NCEP FNL valid at 1800 UTC 11 Apr 2001. (b) As in Fig. 4b but from the NCEP FNL analysis valid at 1800 UTC 11 Apr 2001.

energetically linked by AGF is indicative of the presence of a wave packet, a fact to be confirmed in section 5e. By  $D - 3$ , a net transfer of energy from center A to centers B and C has occurred (Fig. 7b). Developing EKE center C grows in size over this 24-h period but does not grow in intensity. The AGF vectors suggest that there is downstream dispersion of energy, albeit weak, away from center C across the central United States by this time. The majority of the energy dispersion, however, is involved in recirculation between centers B and C. This recirculation effect has been observed in previous studies (e.g., Orlanski and Sheldon

1995) and is believed to retard the decay of EKE maxima that would otherwise occur through AGF divergence. At  $D - 2$  (Fig. 7c), centers B and C remain close to their prior locations, with a net energy transfer occurring from B to C. The EKE centers begin an eastward motion on 6 April (Fig. 7d), and it is on this day that the associated surface cyclone begins to form. Center B is very weak by this time, having dispersed its energy to C. Also observed at this time is a reduction of recirculation and an opening of the closed low in the height contours. Downstream dispersion develops rapidly around this time, with new centers forming over the

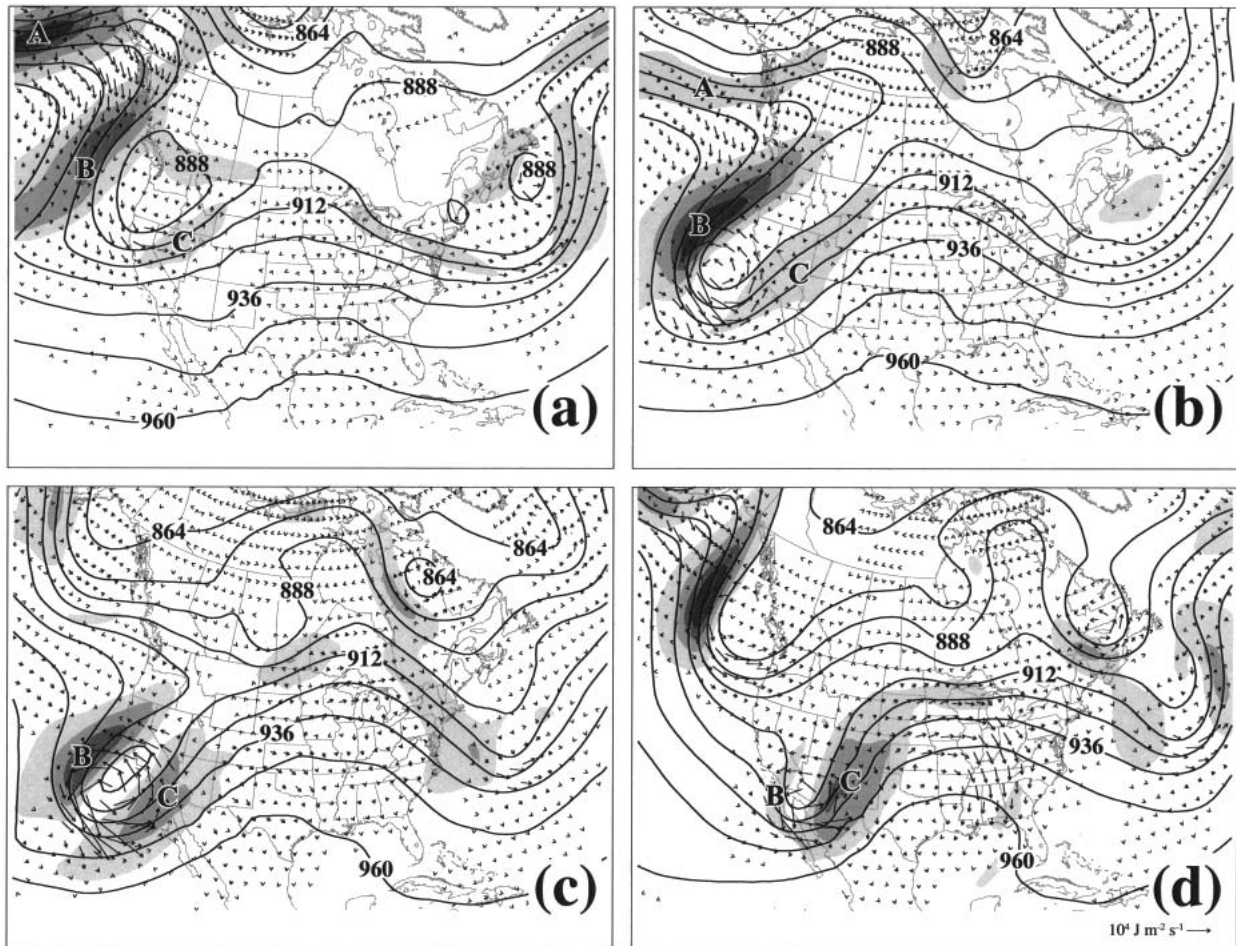


FIG. 7. The 300-hPa geopotential heights, vertically averaged EKE, and vertically averaged AGF vectors at (a) 1200 UTC 3 Apr 2001 ( $D - 4$ ), (b) 1200 UTC 4 Apr ( $D - 3$ ), (c) 1200 UTC 5 Apr ( $D - 2$ ), (d) 1200 UTC 6 Apr ( $D - 1$ ), (e) 0000 UTC 7 Apr ( $D - 0.5$ ), (f) 1200 UTC 7 Apr ( $D0$ ), (g) 0000 UTC 8 Apr ( $D + 0.5$ ), and (h) 1200 UTC 8 Apr ( $D + 1$ ). Geopotential heights (solid lines) are contoured every 12 dam. Vertically averaged EKE is shaded every  $100 \text{ J m}^{-3}$  beginning at  $100 \text{ J m}^{-3}$ . AGF vector scale ( $\text{J m}^{-2} \text{ s}^{-1}$ ) is given by the reference vector on the bottom right of (d) and (h). Boldface letters refer to individual EKE centers referred to in the text.

Great Lakes (D) and the Southeast (E) over the next 12 h (Fig. 7e). Despite no longer having an upstream source of EKE (notice the lack of an energetic connection between C and its closest upstream neighbor off the Washington–Oregon coast), center C maintains its integrity on 7 April (Figs. 7e,f). However, the robust energy dispersion apparent throughout this day, only a small part of which is involved in recirculation, eventually leads to the weakening of C during 8 April (Figs. 7g,h). In response, center D intensifies, becoming associated with an intense cutoff low well off the East Coast.

#### b. Storm-2 EKE evolution

Storm 2 also develops as a result of energy dispersion from two upstream EKE centers (Fig. 8). At  $D - 2.5$ , which corresponds to 0600 UTC 9 April, these centers are located along the Alaska Panhandle (F) and just off the Oregon coast (G) (Fig. 8a). Center H, to be asso-

ciated with storm 2, is barely detectable at this time but develops over the balance of the day (Fig. 8b). Two differences between the evolutions of storms 1 and 2 become apparent on 10 April (Figs. 8b,c). First, unlike center A, center F never completely dissipates, probably because of the influx of energy dispersed toward it by yet another EKE center moving into the Gulf of Alaska. Second, there is little if any downstream dispersion away from H on this day, even at  $D - 1$  (Fig. 8c). Rather, the AGF leaving H is involved completely in recirculation. A comparison of this with the pattern at  $D - 1$  for storm 1 (Fig. 7d) shows stark differences. Center G dissipates on 11 April (Fig. 8d), but the recirculation remains vigorous throughout the day (Fig. 8e). Notable downstream dispersion away from H commences on this day, but even at  $D0$  (Fig. 8e) it is meager in comparison with that observed at  $D0$  for storm 1 (Fig. 7f). Observe that center F remains strong at  $D0$  and is located just upstream of H.

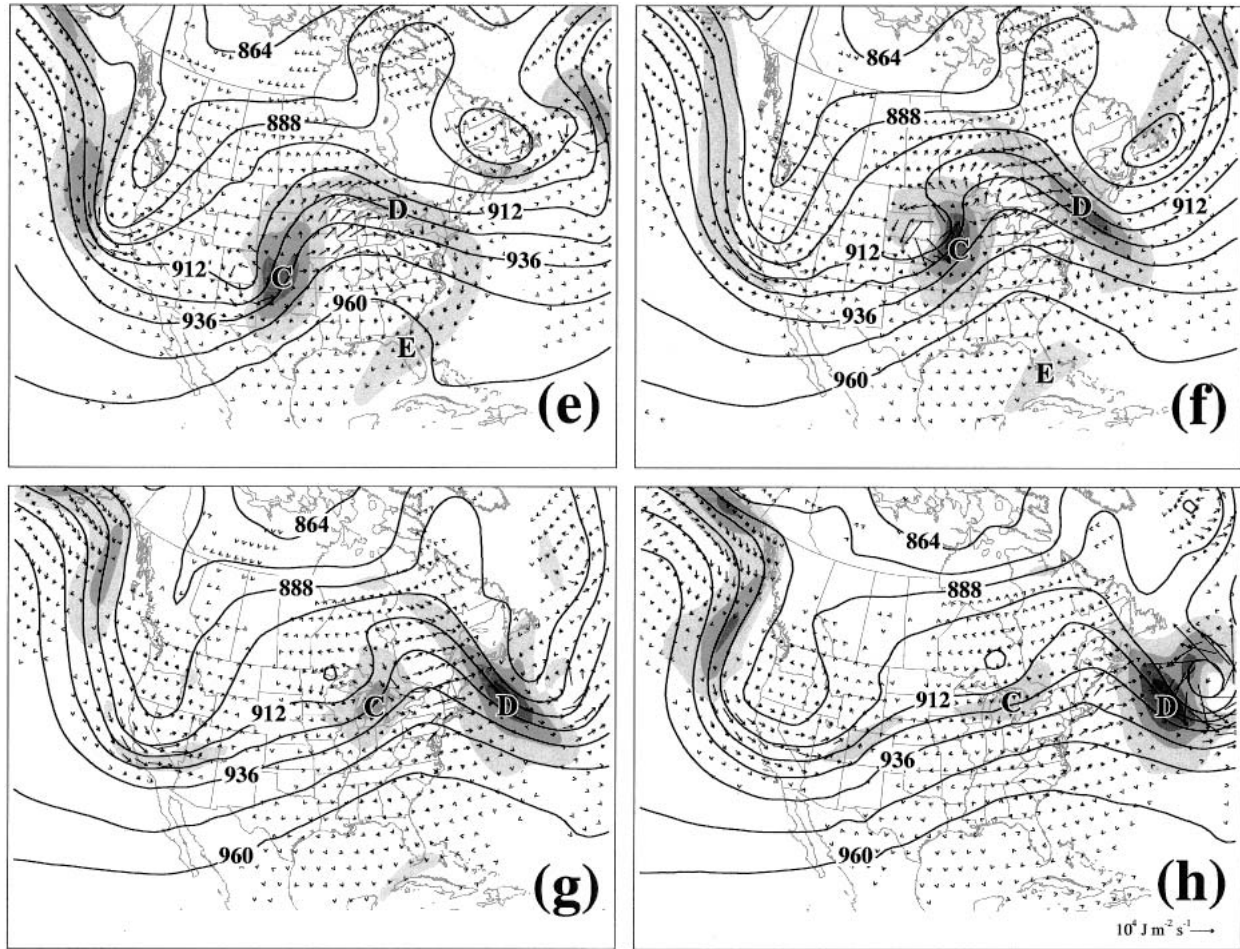


FIG. 7. (Continued)

Key differences between the two storms' evolutions are also apparent in the range from D0 to D + 1 (Figs. 8e–g). The first difference between the storms is the continued presence of recirculation near storm 2, even out to D + 1 (Fig. 8g). In contrast, storm 1 had only minor recirculation after about D + 0.5 (Figs. 7f–h). The second difference is that center H absorbs center F completely over the period from D0 to D + 1. Recall that the nearest upstream EKE maximum to center C did *not* supply it with energy during the parallel period for storm 1. As a result, H is much more robust than C at D + 1 (cf. Figs. 7h and 8g), even though H by this time radiates substantial energy downstream. Once this new energy source has been depleted, center H begins to dissipate on 13 April (Fig. 8h). Note that, just as in the case of storm 1, the result of the downstream energy dispersion is the development of a deep low located well off the East Coast.

Thus far, we have seen two main energetics differences that might account for the disparity in the synoptic evolution of the two cyclones. First, the EKE center associated with storm 1 dispersed energy down-

stream much earlier in its evolution than did its counterpart for storm 2. Second, the EKE center associated with storm 2 received an additional influx of energy just after it reached its minimum SLP; no such energy influx occurred to maintain its counterpart for storm 1. Differences in recirculation, which may have enhanced the characteristic differences just mentioned, were also noted. However, the foregoing analysis only qualitatively showed what the AGFC might look like, and the other budget terms were neglected. To support the assertions made thus far, all of the budget terms are now calculated, and the results are quantified through volume integrals.

### c. Storm-1 budget

Plan views of the distribution of the four leading, vertically integrated EKE tendency terms for Storm 1 at D0 are given in Fig. 9. Note that different panels use different contour intervals depending on the term being plotted. As would be expected with a cyclone that has been rapidly deepening, baroclinic conversion is intense across the northern region of the energy center

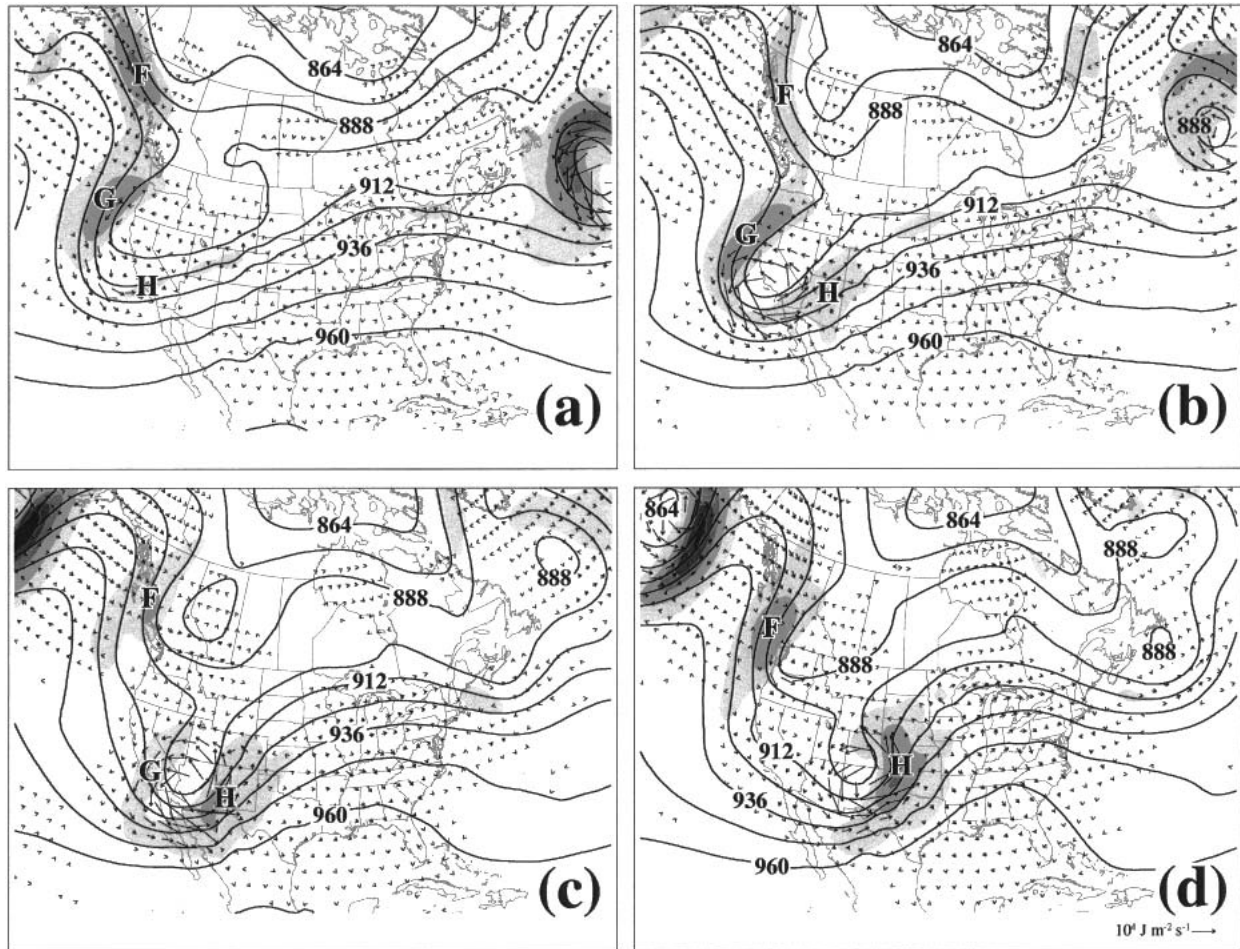


FIG. 8. As in Fig. 7 but for (a) 0600 UTC 9 Apr 2001 ( $D - 2.5$ ), (b) 0000 UTC 10 Apr ( $D - 1.75$ ), (c) 1800 UTC 10 Apr ( $D - 1$ ), (d) 0600 UTC 11 Apr ( $D - 0.5$ ), (e) 1800 UTC 11 Apr ( $D0$ ), (f) 0600 UTC 12 Apr ( $D + 0.5$ ), (g) 1800 UTC 12 Apr ( $D + 1$ ), and (h) 0600 UTC 13 Apr ( $D + 1.5$ ).

(Fig. 9b), north and east of the surface cyclone. Notice, however, the nearly equal and opposite EKE tendencies provided by AGFC (Fig. 9a). Recirculation results in some of the AGFC canceling itself within the bounding contour (recall Fig. 7f). What remains counteracts the baroclinic generation. With the two main terms roughly canceling each other, it is left to the minor terms such as friction (Fig. 9c) and time-mean stress (TMS)(Fig. 9d) to begin the decay of C.

Figure 10 presents a time series of the magnitude of the volume-integrated EKE center associated with storm 1 (center C) and the sea level pressure trace of the storm. Two growth spurts of EKE are apparent. The first occurs between 1200 UTC 3 April and 1200 UTC 4 April, and the second occurs between 0000 UTC 5 April and 0000 UTC 6 April. Note that a well-defined surface cyclone does not even exist until 12 h after the second growth spurt has ended. Furthermore, the EKE center begins its decay 6 h before storm 1 has reached maximum intensity at the surface. This time lag is ob-

served throughout the speedy decay of both the surface cyclone and its associated EKE center.

A time series of the volume-integrated EKE budget terms, normalized through division by the volume-integrated EKE at each time and presented in terms of per-day growth rates, is shown in Fig. 11. The purpose of the normalization is to prevent the results from varying across orders of magnitude throughout the evolution of the storm, so that comparisons between different stages of the life cycles of the EKE centers under consideration can be made more easily. The results appear only when the volume-integrated EKE is greater than 1 EJ ( $10^{18}$  J) to ensure that the bounding contour is large enough to produce sensible results.

During the early growth stages of the EKE center, AGFC was positive, peaking at two times corresponding to the two growth spurts. AGFC was not the only factor, though, since at various times both barotropic conversion and time-mean stress were the primary contributors to EKE growth. Note that TMS also inhibited

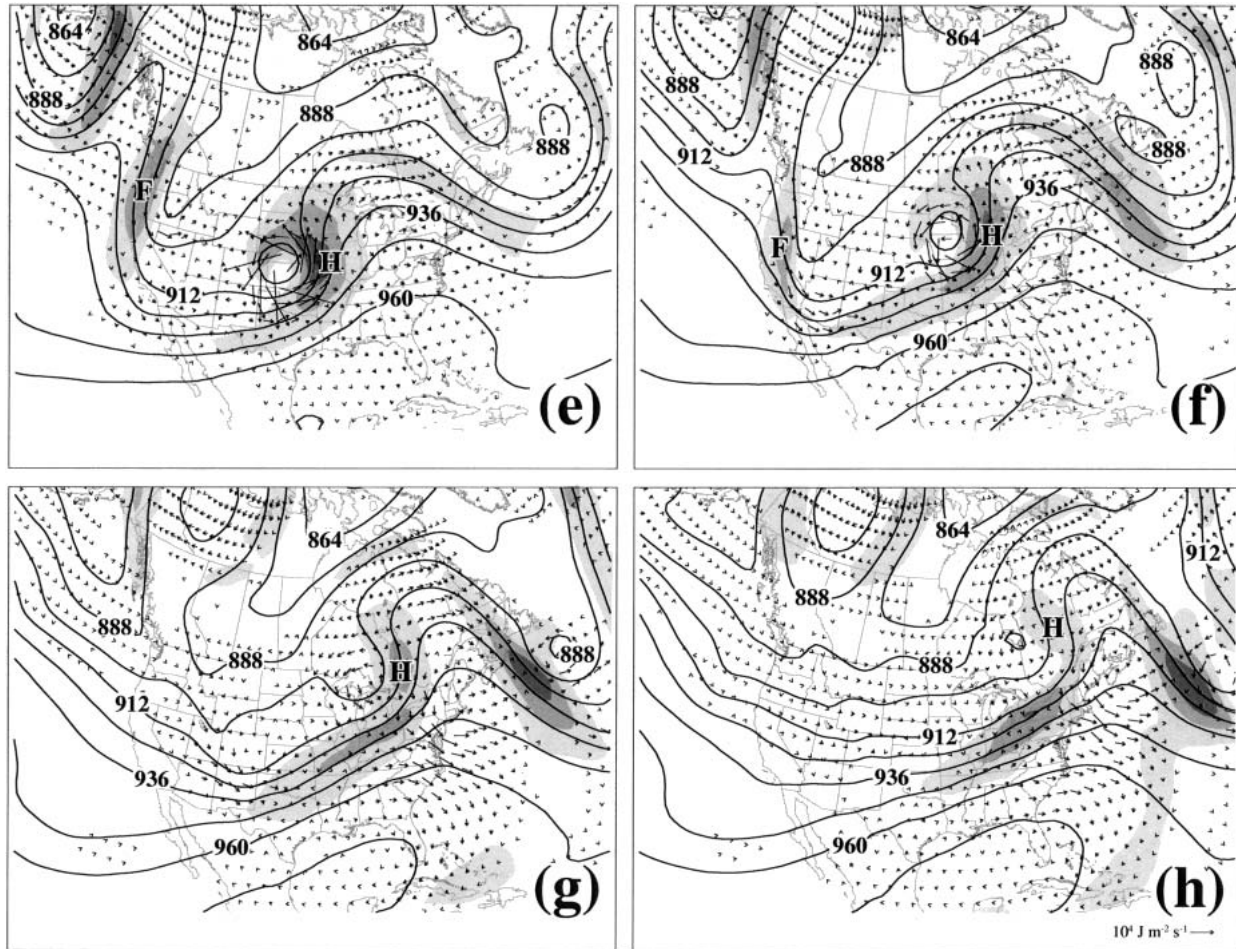


FIG. 8. (Continued)

growth early on, however. Early on 5 April, baroclinic generation acted in opposition to the EKE center's growth but could not prevent the explosive growth of the center. During the rapid development of storm 1 at the surface between 1200 UTC 6 April and 1200 UTC 7 April, AGFC and baroclinic generation become the most dominant processes. The apparent inverse relationship between the two processes suggests that almost all of the EKE generated by baroclinic processes during this period was immediately dispersed through AGFC. These two processes maintain a balance while the volume-integrated EKE is at a plateau but lose that balance once storm 1 reaches its minimum SLP at 1200 UTC 7 April. Over the next 12 h, the cyclone decays most rapidly in terms of both EKE and SLP. From the budget analysis, we see it is during this time that friction and time-mean stress, combined with AGFC, overwhelm the positive contributions from baroclinic and barotropic generation of EKE. For instance, at 1200 UTC 7 April, AGFC, friction, and TMS sum to  $-3.2 \text{ day}^{-1}$  while baroclinic and barotropic generation sum to  $2.7 \text{ day}^{-1}$ . This disparity grows by about  $0.5 \text{ day}^{-1}$

over each of the next two times. Last, note that the residual has little bias, indicating that the friction term as calculated is close to the true frictional dissipation.

#### d. Storm-2 budget

A similar analysis was undertaken for storm 2. Figure 12 illustrates the most important budget terms at D0 for storm 2. As was the case for storm 1, there is a region of AGF divergence over the Upper Midwest (Fig. 12a). However, the divergence is slightly weaker than the baroclinic generation in some locations (Fig. 12b), especially over Missouri. This is in contrast to storm 1 for which the AGF divergence was generally stronger than the collocated baroclinic generation (Figs. 9a,b). Note that as a result of the comparatively weak downstream dispersion from the EKE center associated with storm 2, the downstream EKE center over Quebec, Canada, is much smaller than the equivalent center downstream of storm 1. A large region around storm 2 contains negative tendencies from friction (Fig. 12c). However, there is also a small region in which the friction term is

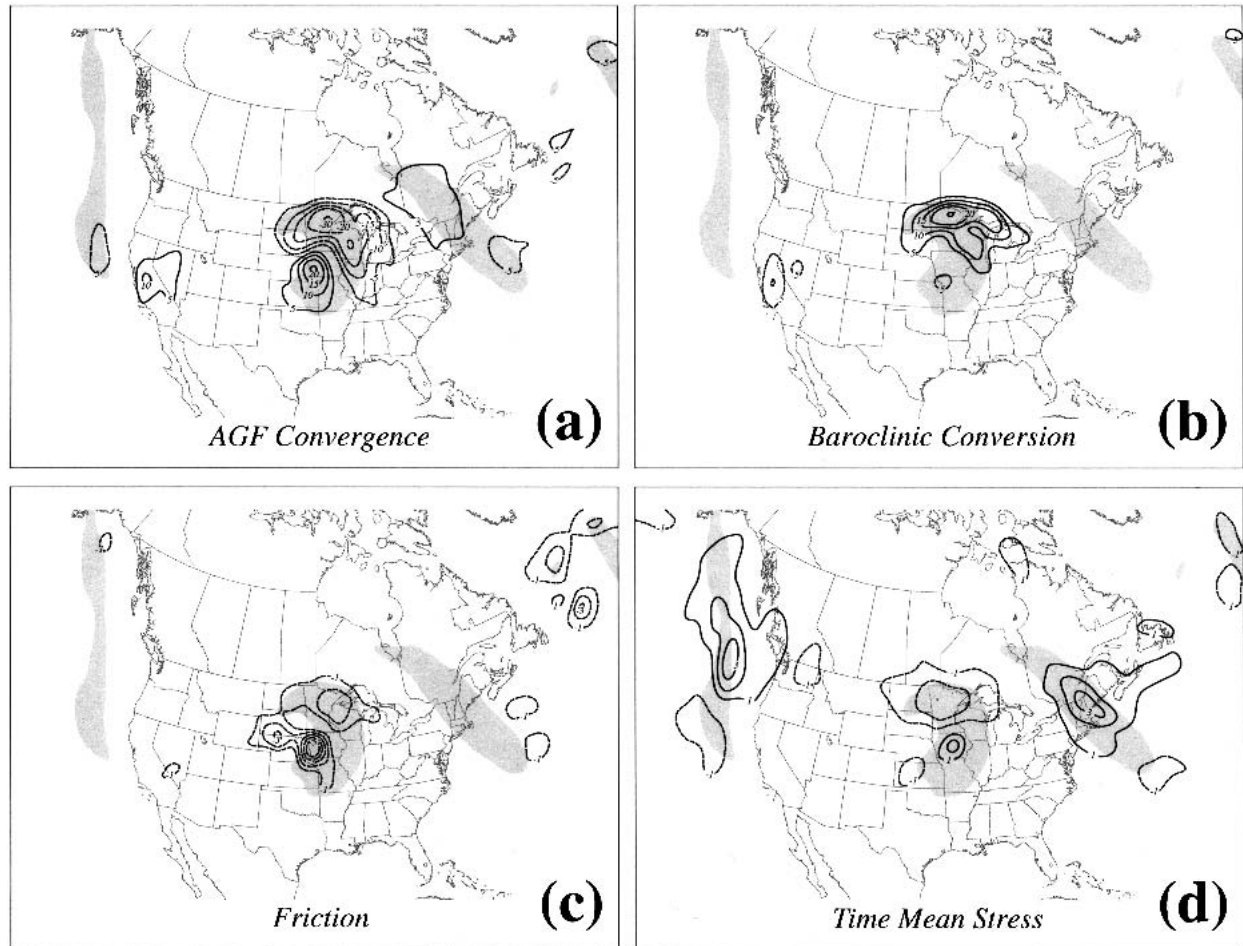


FIG. 9. Vertically averaged EKE tendency terms and EKE at 1200 UTC 7 Apr 2001. Shading represents vertically averaged EKE greater than  $135 \text{ J m}^{-3}$ . (a) Positive (solid lines) and negative (dashed lines) vertically averaged EKE tendency resulting from ageostrophic geopotential flux convergence, contoured every  $5 \text{ mJ m}^{-3} \text{ s}^{-1}$  and beginning at 5 (solid lines) and  $-5$  (dashed lines)  $\text{mJ m}^{-3} \text{ s}^{-1}$ . (b) As in (a), but for EKE tendency arising from baroclinic conversion. (c) As in (a), but for EKE tendency arising from friction, contoured every 1 (solid lines) and  $-1$  (dashed lines)  $\text{mJ m}^{-3} \text{ s}^{-1}$ . (d) As in (c), but for EKE tendency arising from time-mean stress.

positive over Nebraska. This is the most extreme example of positive friction found at any time over the evolution of either storm. The reason for the positive friction is that the winds in the boundary layer flow toward higher heights within this region (not shown). Because the friction term is calculated assuming that all work done by the pressure gradient force within the boundary layer is lost through friction, regions such as this in which the PGF actually does work against the flow result in friction compensating through a positive EKE tendency. In any case, the net friction is clearly negative, as it should be. The advection term is much more strongly negative on the upstream side of storm 2's EKE center than it is positive on the downstream side (Fig. 12d).

A similar comparison between volume-integrated EKE and SLP can be made in the case of storm 2 (Fig. 13). The graph shows that, unlike storm 1, the energy

center associated with storm 2 grows at an almost constant rate over the 36-h period beginning at 0000 UTC 10 April. The EKE center subsequently decays, but the decay is arrested between 0600 UTC 12 April and 1800 UTC 12 April, precisely when additional energy was radiated into the system from its close upstream neighbor. After that point, the energy center decays swiftly. The SLP and EKE of storm 2 are highly synchronized, in contrast to storm 1. Storm 2 reached its maximum intensity at the same time as the associated EKE center, and the hump in the EKE around 1800 UTC 12 April is followed 12 h later by a small decrease in SLP during the decay. This lag is a possible indication that the EKE increase resulting from AGFC over Texas and Oklahoma might have contributed to the prolonged nature of storm 2. Although storm 2 was clearly not decaying as quickly as storm 1 before that point, the additional energy provided by the upstream system appears to have

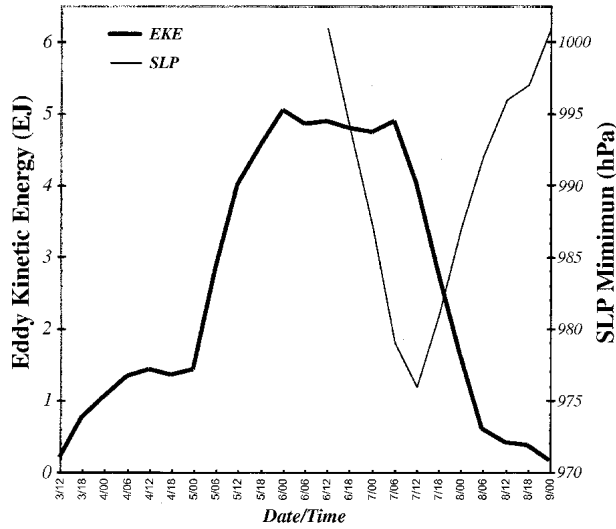


FIG. 10. Evolution of volume-integrated EKE and minimum sea level pressure associated with storm 1. Thick solid line is EKE (EJ; left axis). Thin solid line is SLP (hPa; right axis). Date and time are indicated using the convention DD/HH, where DD refers to the calendar date in Apr 2001 and HH refers to the hour (UTC).

made the differences between the two storms even more apparent.

A look at the volume-integrated budget terms (Fig. 14) reveals that the first part of the growth phase of the EKE center was dominated by AGFC, whereas the last 12 h of growth (up to 1800 UTC 11 April) were dominated by baroclinic generation. Storm 2's EKE center enjoyed a long period of growth from baroclinic generation not fully counteracted out by AGFC over the next 24 h. It was not until 1800 UTC 12 April, after the upstream energy had been ingested into the system, that these two terms became equal in magnitude. The strongly negative advection noted above shows up at 0600 and 1200 UTC 11 April as the most decay-inducing process at those times. Friction was negative throughout the evolution, despite the small region of positive friction previously mentioned. During the fastest decay (last two times in Fig. 14), AGFC was dominant over baroclinic generation, and a menagerie of minor terms (TMS, friction, and even curvature) added up to cancel positive contributions from barotropic growth. Notice that the barotropic generation term was positive throughout the decay stage of both storms,

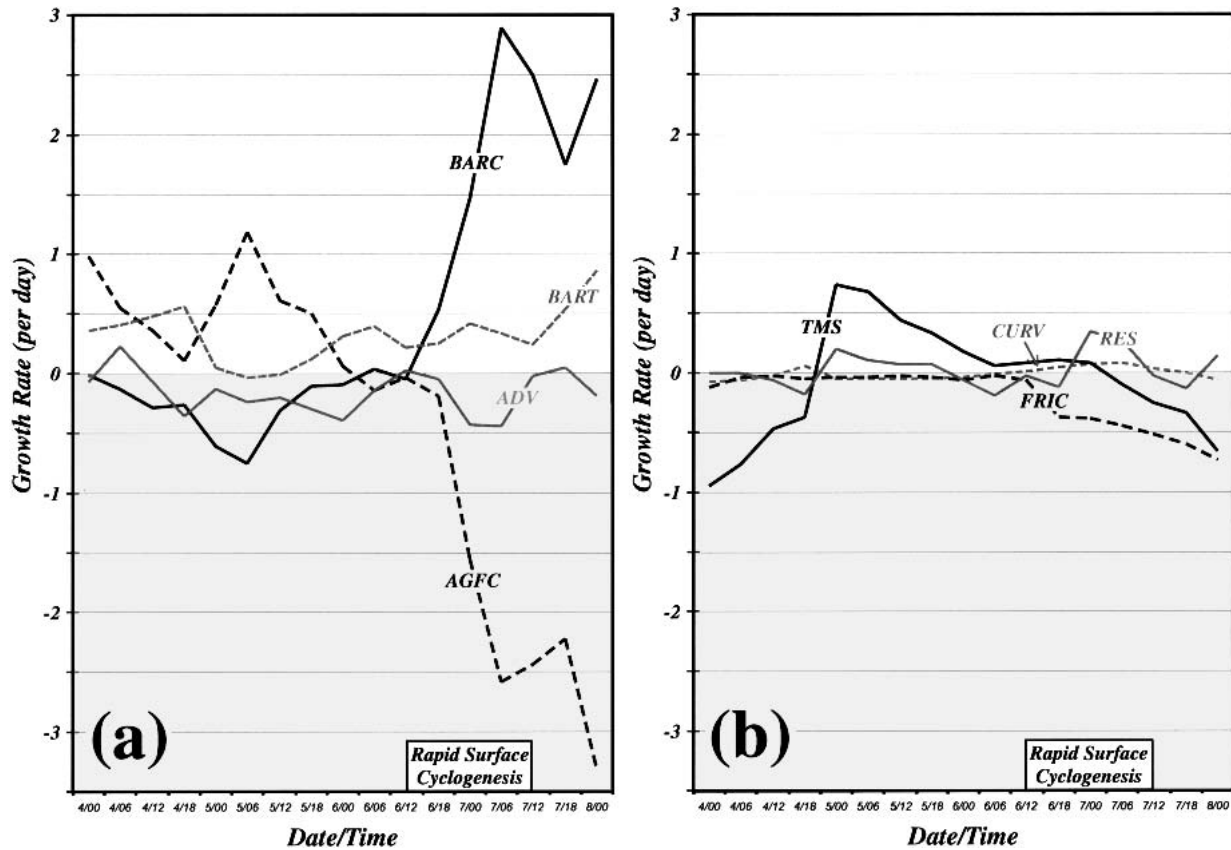


FIG. 11. Volume-integrated EKE tendency terms, quantified as growth rates per day, over the life cycle of storm 1: (a) baroclinic conversion (BARC; solid black line), AGFC (black dashed line), EKE advection (ADV; solid gray line), and barotropic conversion (BART; dashed gray line); (b) time mean stress (TMS; solid black line), friction (FRIC; dashed black line), residual (RES; solid gray line), and curvature (CURV; dashed gray line). The date/time convention is as in Fig. 10. The period of most rapid surface cyclogenesis is indicated along the time axes.

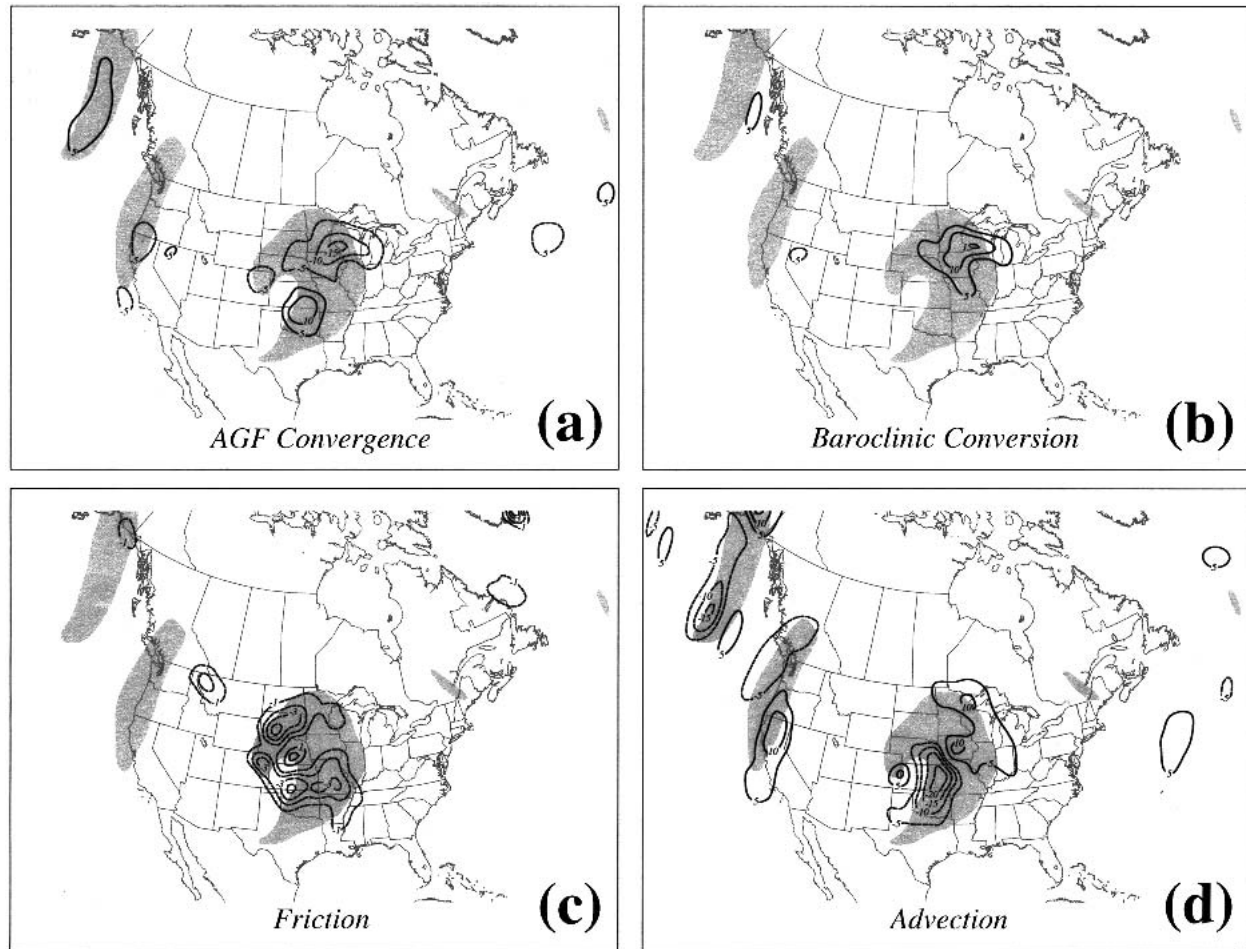


FIG. 12. As in Fig. 9 but at 1800 UTC 11 Apr 2001, except that (d) is for EKE tendency arising from advection.

contradicting the suggestion of Simmons and Hoskins (1978) that baroclinic systems decay barotropically.

#### e. Hovmöller diagrams

Examination of the so-called wave-packet envelope function can help to determine whether either storm was associated with a long-lived wave packet. This function was first used by Chang and Yu (1999) to pick out wave packets in real data<sup>4</sup> and has subsequently been used by Chang (2000, 2001). To calculate the envelope function, the eddy meridional wind at 300 hPa is assumed to be of the form

$$v(x, t) = \text{Re}[E(x, t)e^{ikx}], \quad (6)$$

where  $E$  is the envelope function and  $k$  is the wavenumber of a typical baroclinic wave. The method of complex demodulation recovers  $E$  given  $v$  and  $k$ . Chang

and Yu (1999) report that the envelope function is insensitive to changes in  $k$ . In this study,  $k$  is defined using the values mentioned in Chang (2000), that is, wavenumber 8 at 30°, wavenumber 6 at 60°, and wavenumber 4 at 75°. Zimin et al. (2003) have recently described an alternate method of determining the wave-packet envelope function, but that method is not employed here.

One way to examine wave packets is to use Hovmöller diagrams. This method is advantageous because it allows for an efficient comparison of the relationships the two storms may have had with wave packets. It also can provide insight about some of the EKE budget results discussed previously.

The Hovmöller diagrams presented are derived by taking area-weighted averages along 1°-wide longitudinal strips stretching between 20° and 70°N. Each area-weighted average is constructed using already vertically averaged quantities such as EKE or AGFC. Each longitude is assigned its corresponding area-weighted average value at each time, and the resulting 2D array of data is contoured to produce the diagram. The Hov-

<sup>4</sup> Lee and Held (1993) used a related method to analyze their idealized model results.

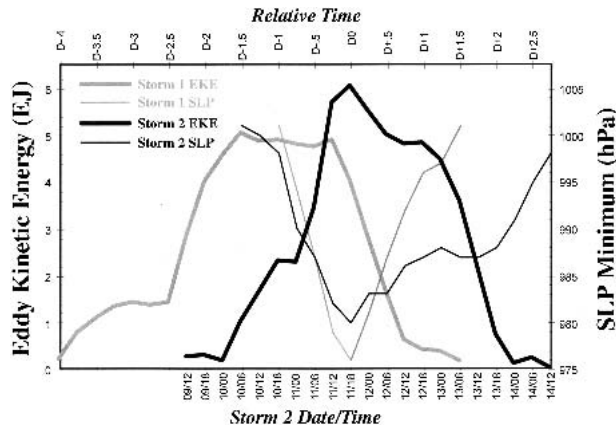


FIG. 13. Comparison of the evolution of volume-integrated EKE and minimum sea level pressure associated with storms 1 and 2. Thick black and gray lines are time series of EKE (EJ; left axis) for storms 2 and 1, respectively. Thin black and gray lines are time series of SLP (hPa; right axis) for storms 2 and 1, respectively. Date and time refer to storm 2 and are indicated using the convention DD/HH, where DD refers to the calendar date in Apr 2001 and HH refers to the hour (UTC). The relative time referred to at the top uses the convention  $D \pm X$  to indicate  $X$  number of days before or after the time of minimum SLP (D0).

möller diagram for the wave-packet envelope function is shown in Fig. 15. To help in interpreting the diagram, “X”s have been placed to illustrate the location at which each storm most rapidly intensified, and plus signs have been placed to indicate the path each storm subsequently took through longitude–time space. Wave packets are clearly seen as strips of elevated envelope function directed from early times and westerly longitudes to later times and easterly longitudes. Unlike in the Southern Hemisphere, where wave packets often circumnavigate the globe (Chang 1999), there is no wave packet that does so over this period.

Both storms appear to be associated with wave packets that originated near  $150^{\circ}\text{E}$  and dissipated around the prime meridian. The locations of the storms relative to the wave packets are remarkably different, however. Storm 1 developed and lived on the upstream edge of its associated wave packet, whereas storm 2 developed in the heart of a wave packet, not substantially weakening until it had moved to that wave packet’s edge. This contrast is consistent with the earlier conclusion that storm 1 began sending a radiative flux of energy downstream much earlier than did storm 2. Such downstream dispersion is to be expected on the upstream side of a wave packet because it is on that side that AGF is strongly divergent on average (Chang 2001, his Fig. 5b).

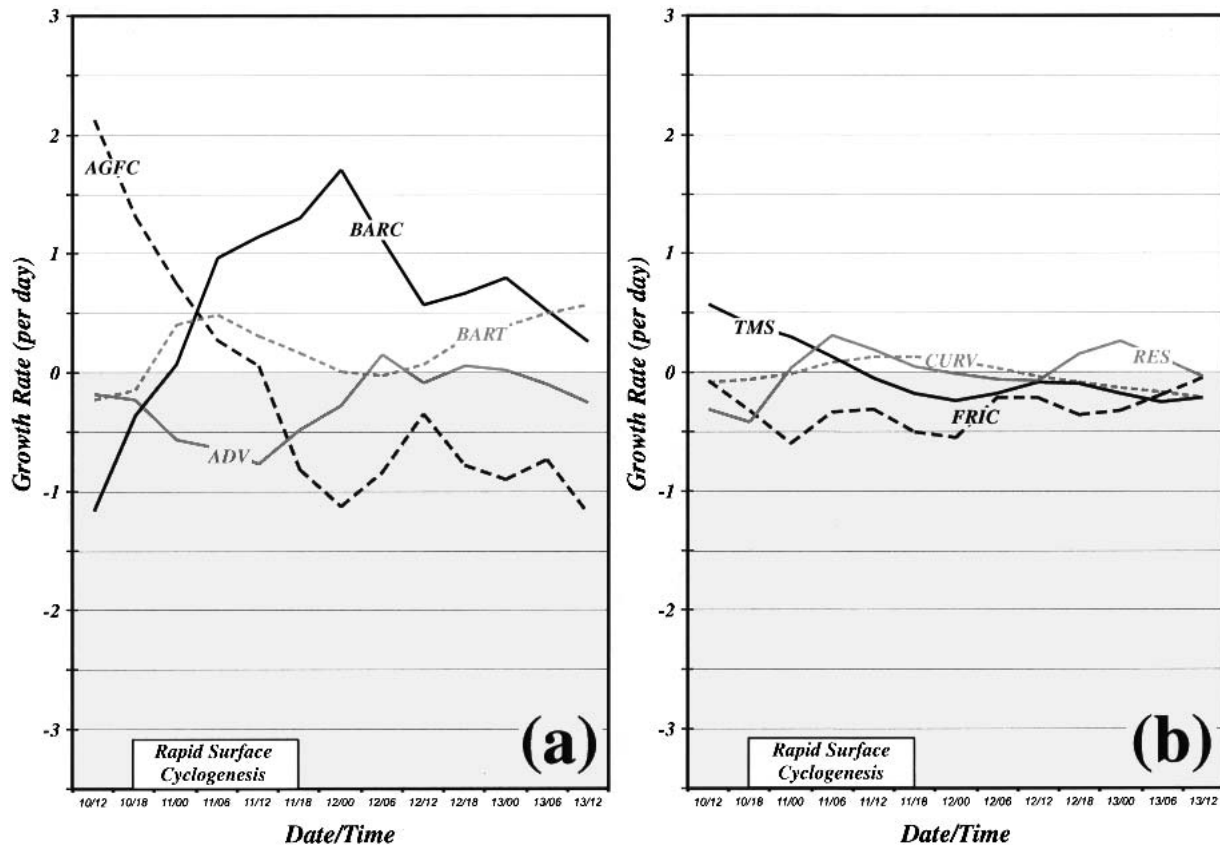


FIG. 14. As in Fig. 11 but for storm 2.

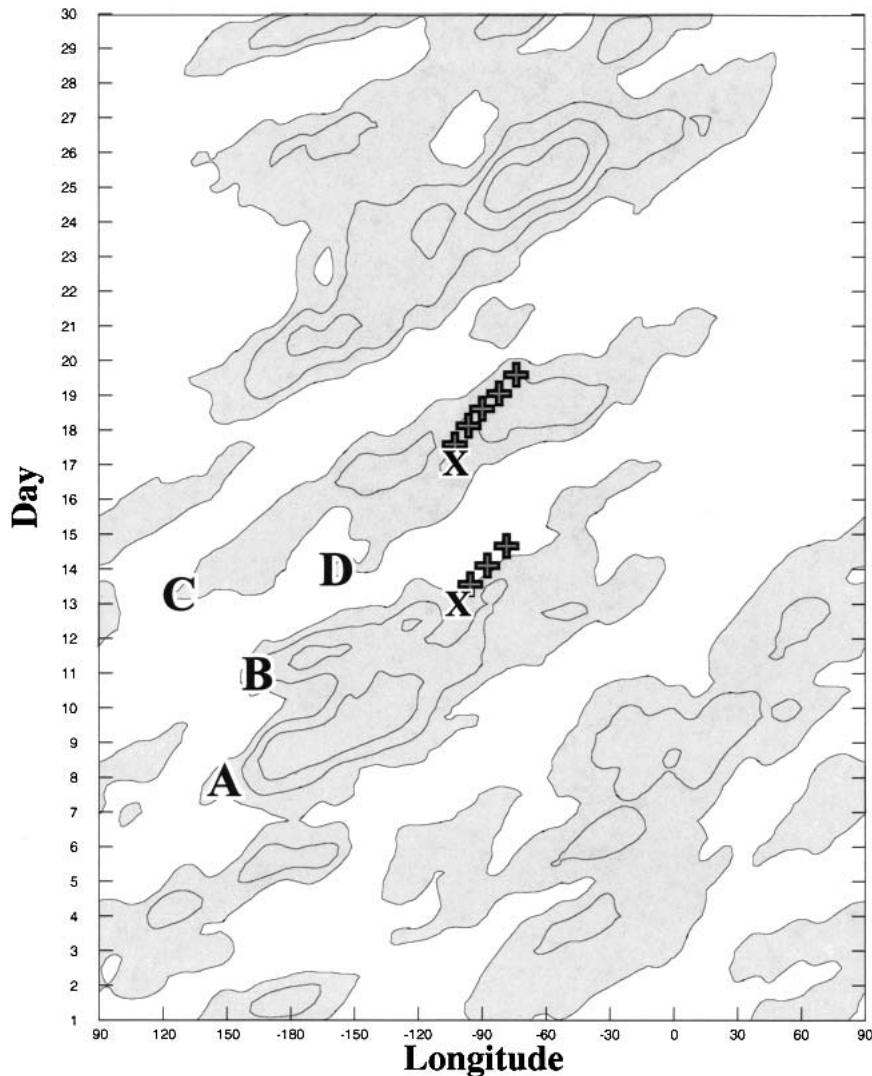


FIG. 15. Hovmöller diagram of the vertically and latitudinally averaged wave-packet envelope function over a 30-day period from 0000 UTC 26 Mar 2001 to 0000 UTC 24 Apr 2001 contoured and shaded every  $4 \text{ m s}^{-1}$ , beginning at  $14 \text{ m s}^{-1}$ . Letter X marks the location of each storm at its most intense phase, and plus signs mark the subsequent longitude-time location of each storm at 12-h intervals. Letters A, B, C, and D are referred to in the text.

Closer inspection reveals a detailed and perhaps convoluted structure to these wave packets. The wave packet associated with storm 1 may be the result of a merger between two wave packets, one that developed on day 8 near  $150^\circ\text{E}$  (A) and one that developed a little farther to the east on day 11 (B). The wave packet associated with storm 2 also shows some evidence of having undergone a merger, with one packet developing at  $120^\circ\text{E}$  on day 13 (C) and a second packet developing near  $150^\circ\text{W}$  on day 14 (D).

The various EKE budget terms can also be displayed in Hovmöller diagram form. Figure 16 presents such diagrams for ageostrophic geopotential flux divergence and baroclinic generation. When downstream development is occurring, a wave packet is characterized by a

train of alternately signed regions of AGFC, as is the case in Fig. 16a. Thus, this diagram can be used to better determine whether and, perhaps, how the wave packet mergers mentioned above actually occurred. Notice that, within wave packet regions, EKE maxima (which are tied to individual ridges and troughs) move eastward more slowly than the wave packets themselves. In addition, the upstream (western) halves of EKE maxima typically are associated with growth from AGFC (in black shading), and the downstream (eastern) halves are typically associated with decay by AGF divergence (in gray shading). This pattern is in accordance with the downstream development paradigm.

Figure 16a reveals that wave packet B did not merge with wave packet A. Instead, it remains distinct almost

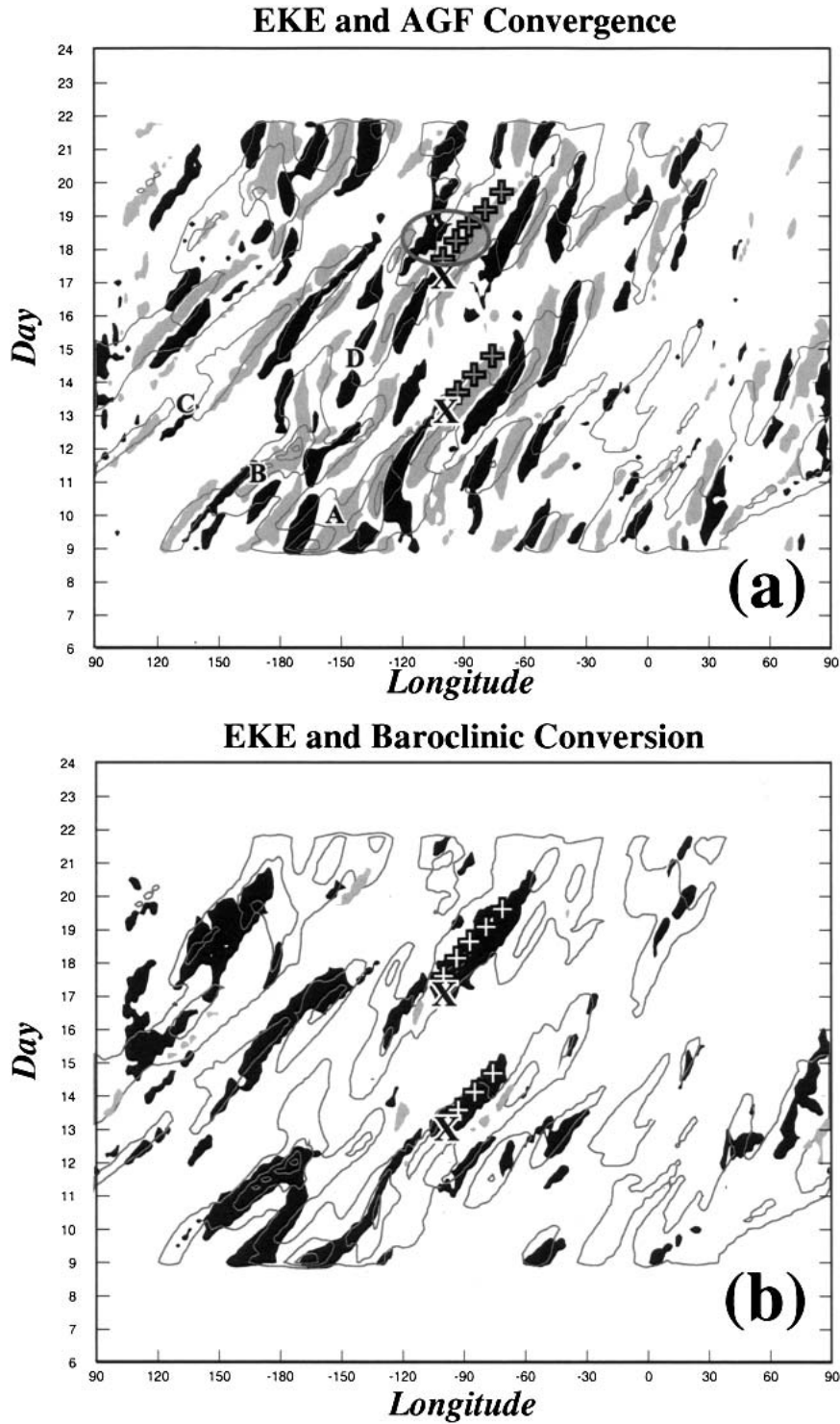


FIG. 16. (a) Hovmöller diagram of EKE and AGFC from 0000 UTC 31 Mar 2001 (day 6) to 0000 UTC 18 Apr 2001 (day 24). EKE is contoured every  $50 \text{ J m}^{-3}$ , starting at  $50 \text{ J m}^{-3}$ . AGF convergence (divergence) of magnitude greater than  $50 \text{ J m}^{-3} \text{ day}^{-1}$  is shaded in black (gray). Letters A, B, C, and D, along with the elliptical region, are referred to in the text. (b) Hovmöller diagram of EKE and baroclinic conversion from 0000 UTC 31 Mar 2001 (day 6) to 0000 UTC 18 Apr 2001 (day 24). EKE is contoured as in (a). Baroclinic conversion magnitudes of greater than  $50 \text{ J m}^{-3} \text{ day}^{-1}$  are shaded black for positive conversion and gray for negative conversion. The letter Xs and plus signs are as in Fig. 15.

30° to the west, dissipating around the time storm 1 does. In contrast, the original wave packet associated with storm 2 (D, which appears to initiate from a long-lasting, slow-moving EKE maxima between 180° and 150°W on day 14) can be seen to merge with the other wave packet (C) in the elliptical region highlighted at day 18 in Fig. 16a. Whereas prior to day 18 there are two distinct trains of alternately positive and negative AGFC (packets C and D), after this point there is only one train, which progresses downstream to about 30°W by day 20. Indeed, it is this merger that allows storm 2 to experience two periods of AGFC associated with energy fluxes dispersed from upstream. This merger also explains why EKE center F survived for such a long time (recall Fig. 8). Just as it was about to dissipate after the first wave packet propagated through it, a second wave packet came along to reenergize it. The wave train associated with this second packet can be traced back to 30°E at day 9. It was simply too weak as it crossed central Asia to show up on the envelope-function diagram (Fig. 15).

In turning now to baroclinic conversion (Fig. 16b), it is clear that baroclinic growth occurred over a longer duration for storm 2 than for storm 1. The timing of the baroclinic growth relative to the EKE maxima is also different between the two storms. A large swath of positive baroclinic conversion covers the entire  $100 \text{ J m}^{-3}$  contour of storm 2's EKE maximum, while less than one-half of the same contour for storm 1's EKE maximum is so covered. This result reflects the fact that the storm-1 surface cyclone developed after its associated EKE maximum had finished development, whereas the storm-2 surface cyclone developed as its associated EKE maximum developed.

## 6. Concluding discussion

Although both the growth and decay of cyclones over central North America have been previously addressed, the techniques used have been based on basic fields such as wind, humidity, and stability (Achter and Horn 1986; Marshment and Horn 1986), quasigeostrophic theory and frontogenesis (Ruscher and Condo 1996a,b), or an extension of the Zwack–Okossi equation (Morris and Smith 2001). Thus, prior studies have not considered possible interactions with other systems upstream or downstream, which are fundamental in the downstream development paradigm of Orlanski and Sheldon (1995). In addition, prior studies performed using local energetics diagnostics have nearly all been based on individual case studies (Orlanski and Katzfey 1991; Orlanski and Sheldon 1995; Chang 2000) or composites (McLay and Martin 2002). The preceding analysis is unique in that it may be the first to have examined differences between the life cycles of consecutive, explosively deepening cyclones from an energetics viewpoint.

The results of the study can be summarized as fol-

lows. First, each storm's associated EKE center grew (decayed) primarily through ageostrophic geopotential flux convergence (divergence), adhering to the downstream development paradigm of Orlanski and Sheldon (1995). Second, storm 1's EKE center reached maximum intensity well before the establishment of the surface cyclone, in contrast to storm 2, whose EKE center intensified simultaneously with the development of the surface cyclone. This difference resulted in the maintenance of storm 2's SLP minimum below 1000 hPa for twice as long as that of storm 1, despite the fact that both storms' EKE centers were equally intense for equal durations. Third, storm 1 developed on the upstream edge of a wave packet, whereas storm 2 developed in the middle of one.

This third element may be a prominent physical factor in the vastly different decay stages experienced by the two storms. By developing on the upstream side of a wave packet, storm 1 was in a favorable position to experience rapid EKE loss immediately through downstream AGF dispersion. This was not the case for storm 2 until much later in its lifetime. Instead, storm 2 developed in the center of a wave packet (which had just undergone a merger), allowing it to receive energy fluxes from two distinct upstream EKE centers during its life cycle.

In addition, although the EKE centers associated with each storm experienced a 3-day period of AGF recirculation, much of the recirculation during storm 1's life cycle occurred before the surface cyclone even formed. The effect of AGF recirculation being to inhibit downstream energy dispersion, the temporal coincidence of this AGF recirculation with the surface development of storm 2 is also consistent with the slower decay of that storm.

Precisely why storm 1 took so long to appear at the surface relative to the life cycle of its associated EKE maximum remains an unanswered question. In their modeling study, Orlanski and Sheldon (1993) suggest that while interaction with orography disrupted the surface development of a cyclone, it left the EKE structure largely unchanged. Because the EKE center associated with storm 1 developed in a location slightly to the west of storm 2's EKE center and because it moved more slowly initially, one possibility is that orographic disruption of the surface development may have played a role in delaying the development of storm 1 at the surface. In fact, Orlanski and Sheldon (1993, p. 2941) note that downstream dispersion of AGF contributed to the decay of their system very early in its life cycle. This hypothesis may be testable through a modeling study of both cyclones with orography removed, but that will be left for future work.

This study also found that barotropic processes played no significant role in the decay of these two cyclones, contrary to the suggestion of Simmons and Hoskins (1978). However, as Orlanski and Chang (1993) elucidated, the Simmons and Hoskins (1978) re-

sults were based on a normal-mode analysis, rendering the growth or decay of disturbances through energy transfer between systems impossible. Because each disturbance in the Simmons and Hoskins (1978) study had identical disturbances both upstream and downstream of itself, energy gained from the upstream system was equally lost to the downstream system. Similar limitations in the idealized life cycle studies of Thorncroft et al. (1993) muddy comparison of our real cases with their LC1 and LC2 cases. It is only in the absence of symmetry [as in a follow-up study by Simmons and Hoskins (1979), or in real-world cases] that net energy transfers from one system to another can occur. Thus, the results presented here provide additional evidence that intersystem net energy transfer, rather than eddy-mean flow interaction, is of primary importance during the development and decay of individual systems, particularly when wave packets are present.

Local energetics diagnostics present just one way of examining energy transfers over the life cycles of midlatitude cyclones. An alternative view might be to examine the budget of wave activity (Andrews et al. 1987, chapter 3) or to employ the generalized Eliassen–Palm (EP) flux diagnostics developed by Plumb (1986) or Trenberth (1986). Whether these viewpoints would add any insight into the evolution of the two cyclones studied herein is an open question. Another unresolved question concerns the importance of the second influx of energy from upstream to the maintenance of storm 2. This issue could be examined through a modeling study in which the upstream EKE center (or perhaps a potential vorticity anomaly associated with that center) is removed from the initial conditions. Such an experiment is left for future work. Last, though midlatitude cyclones are not always associated with coherent wave packets, this study suggests that, for those that are, the location of the cyclone within its wave packet profoundly affects the speed at which the cyclone decays. Of course, this result is based on a meager sample size of two (daily perusal of real-time local energetics diagnostics, available online at <http://speedy.aos.wisc.edu/~sgdecker/realtime.html>, suggests that this is likely a general result). Therefore, additional examples of cyclone decay should be examined both to determine the robustness of this result and to promote a more comprehensive understanding of midlatitude cyclolysis.

*Acknowledgments.* This work presents a portion of the M.S. thesis of the first author. Constructive comments made by Drs. Michael Morgan and Matt Hitchman enhanced the text. The National Science Foundation, under Grant ATM-0202012, supported this research. Valuable comments from three anonymous reviewers greatly enhanced the presentation.

#### REFERENCES

- Achter, T. H., and L. H. Horn, 1986: Spring season Colorado cyclones. Part I: Use of composites to relate upper and lower tropospheric wind fields. *J. Climate Appl. Meteor.*, **25**, 732–743.
- Andrews, D. G., J. R. Holton, and C. B. Leovy, 1987: *Middle Atmosphere Dynamics*. Academic Press, 489 pp.
- Chang, E. K. M., 1999: Characteristics of wave packets in the upper troposphere. Part II: Seasonal and hemispheric variations. *J. Atmos. Sci.*, **56**, 1729–1747.
- , 2000: Wave packets and life cycles of troughs in the upper troposphere: Examples from the Southern Hemisphere summer season of 1984/85. *Mon. Wea. Rev.*, **128**, 25–50.
- , 2001: The structure of baroclinic wave packets. *J. Atmos. Sci.*, **58**, 1694–1713.
- , and I. Orlanski, 1993: On the dynamics of a storm track. *J. Atmos. Sci.*, **50**, 999–1015.
- , and —, 1994: On energy flux and group velocity of waves in baroclinic flows. *J. Atmos. Sci.*, **51**, 3823–3828.
- , and D. B. Yu, 1999: Characteristics of wave packets in the upper troposphere. Part I: Northern Hemisphere winter. *J. Atmos. Sci.*, **56**, 1708–1728.
- Charney, J. G., 1947: The dynamics of long waves in a baroclinic westerly current. *J. Meteor.*, **4**, 135–162.
- Eady, E. T., 1949: Long waves and cyclone waves. *Tellus*, **1**, 33–52.
- Konrad, C. E., II, and S. J. Colucci, 1988: Synoptic climatology of 500 mb circulation changes during explosive cyclogenesis. *Mon. Wea. Rev.*, **116**, 1431–1443.
- Kung, E. C., 1977: Energy source in middle-latitude synoptic-scale disturbances. *J. Atmos. Sci.*, **34**, 1352–1365.
- Kutzbach, G., 1979: *Thermal Theory of Cyclones: A History of Meteorological Thought in the Nineteenth Century*. Amer. Meteor. Soc., 254 pp.
- Lackmann, G. M., D. Keyser, and L. F. Bosart, 1999: Energetics of an intensifying jet streak during the Experiment on Rapidly Intensifying Cyclones over the Atlantic (ERICA). *Mon. Wea. Rev.*, **127**, 2777–2795.
- Lee, S., and I. M. Held, 1993: Baroclinic wave packets in models and observations. *J. Atmos. Sci.*, **50**, 1413–1428.
- Marshment, R. A., and L. H. Horn, 1986: Spring season Colorado cyclones. Part II: Composites of atmospheric moisture and moist static stability. *J. Climate Appl. Meteor.*, **25**, 744–752.
- McLay, J. G., and J. E. Martin, 2002: Surface cyclolysis in the North Pacific Ocean. Part III: Composite local energetics of tropospheric-deep cyclone decay associated with rapid surface cyclolysis. *Mon. Wea. Rev.*, **130**, 2507–2529.
- Morris, W. E., Jr., and P. J. Smith, 2001: Cyclolysis: A diagnosis of two extratropical cyclones. *Mon. Wea. Rev.*, **129**, 2714–2729.
- Namias, J., and P. F. Clapp, 1944: Studies of the motion and development of long waves in the westerlies. *J. Meteor.*, **1**, 57–77.
- NCDC, 2001: *Storm Data*. Vol. 43, No. 4, 260 pp. [Available from National Climatic Data Center, 151 Patton Ave., Asheville, NC 28801.]
- Orlanski, I., and J. Katzfey, 1991: The life cycle of a cyclone wave in the Southern Hemisphere. Part I: Eddy energy budget. *J. Atmos. Sci.*, **48**, 1972–1998.
- , and E. K. M. Chang, 1993: Ageostrophic geopotential fluxes in downstream and upstream development of baroclinic waves. *J. Atmos. Sci.*, **50**, 212–225.
- , and J. Sheldon, 1993: A case of downstream baroclinic development over western North America. *Mon. Wea. Rev.*, **121**, 2929–2950.
- , and —, 1995: Stages in the energetics of baroclinic systems. *Tellus*, **47A**, 605–628.
- Petterssen, S., and S. J. Smebye, 1971: On the development of extratropical cyclones. *Quart. J. Roy. Meteor. Soc.*, **97**, 457–482.
- Plumb, R. A., 1986: Three-dimensional propagation of transient quasi-geostrophic eddies and its relationship with the eddy forcing of the time-mean flow. *J. Atmos. Sci.*, **43**, 1657–1678.

- Ruscher, P. H., and T. P. Condo, 1996a: Development of a rapidly deepening extratropical cyclone over land. Part I: Kinematic aspects. *Mon. Wea. Rev.*, **124**, 1609–1632.
- , and —, 1996b: Development of a rapidly deepening extratropical cyclone over land. Part II: Thermodynamic aspects and the role of frontogenesis. *Mon. Wea. Rev.*, **124**, 1633–1647.
- Sanders, F., and J. R. Gyakum, 1980: Synoptic-dynamic climatology of the “bomb.” *Mon. Wea. Rev.*, **108**, 1589–1606.
- Simmons, A. J., and B. J. Hoskins, 1978: Life cycles of some nonlinear baroclinic waves. *J. Atmos. Sci.*, **35**, 414–432.
- , and —, 1979: Downstream and upstream development of unstable baroclinic waves. *J. Atmos. Sci.*, **36**, 1239–1254.
- Thorncroft, C. D., B. J. Hoskins, and M. E. McIntyre, 1993: Two paradigms of baroclinic-wave life-cycle behavior. *Quart. J. Roy. Meteor. Soc.*, **119**, 17–55.
- Trenberth, K. E., 1986: Assessment of the impact of transient eddies on the zonal flow during a blocking episode using localized Eliassen–Palm flux diagnostics. *J. Atmos. Sci.*, **43**, 2070–2087.
- Volkert, H., 1999: Components of the Norwegian cyclone model: Observations and theoretical ideas in Europe prior to 1920. *The Life Cycles of Extratropical Cyclones*, M. A. Shapiro and S. Grønås, Eds., Amer. Meteor. Soc., 15–28.
- Zimin, A. V., I. Szunyogh, D. J. Patil, B. R. Hunt, and E. Ott, 2003: Extracting envelopes of Rossby wave packets. *Mon. Wea. Rev.*, **131**, 1011–1017.